Developments in the Built Environment 28 (2026) 101049



Contents lists available at ScienceDirect

Developments in the Built Environment

journal homepage: www.sciencedirect.com/journal/developments-in-the-built-environment



Effects of thermo-activation on the aqueous carbonation behavior of calcium silicate hydrate: A multi-scale X-ray scattering and nano-CT study

Sumin Im [a,b], Seongmin Cho [a], Gyeongryul Kim [c], Manabu Kanematsu [d], Satoshi Morooka [e], Nishio Yuhei [d], Akihiko Machida [f], Aki Tominaga [e], Seungjun Kwon [g], Sungchul Bae [a,*]

[a] Department of Architectural Engineering, Hanyang University, Seoul, 04763, Republic of Korea
[b] Department of Civil and Environmental Engineering, University of Michigan, Ann Arbor, MI, 48109, United States
[c] Department of Civil and Environmental Engineering, University of Illinois at Urbana-Champaign Newmark 2145A, 205 N. Mathew, Urbana, IL, 61801, United States
[d] Department of Architecture and Building Engineering, Faculty of Science and Technology, Tokyo University of Science, 2641 Yamazaki, Chiba, 278-8510, Japan
[e] Materials Science Research Center, Japan Atomic Energy Agency, Kouto, Hyogo, 679-5148, Japan
[f] Synchrotron Radiation Research Center, National Institutes for Quantum Science and Technology, Hyogo, 679-5148, Japan
[g] Department of Civil and Environmental Engineering, Hannam University, Daedeok-gu, Daejeon, Republic of Korea

ARTICLE INFO

Keywords:
Calcium silicate hydrate
Thermo-activation
Aqueous carbonation
Pair distribution function
Fractal structure
X-ray nanoimaging
Recycled cementitious materials

ABSTRACT

This study investigates the early-stage aqueous carbonation behavior of thermo-activated calcium silicate hydrate (C-S-H), focusing on the temperature-dependent structural evolution across dehydration (105 °C), decomposition (400 °C), and recrystallization (600 °C) stages, relevant to the valorization of recycled cement pastes and CO_2 mineralization. Multiscale characterization was performed using synchrotron wide-angle and small-angle X-ray scattering combined with pair distribution function (PDF) and fractal analyses, respectively, and X-ray nanoimaging (XNI). Carbonation predominantly affected C-S-H at the dehydration and decomposition stages, whereas β-wollastonite became the primary reactive phase at the recrystallization stage, resulting in increased calcite formation. The PDF analysis revealed that the carbonation-induced structural rearrangement was more pronounced at longer length scales in the crystalline pyrolyzed phases. The fractal and XNI analyses indicated that agglomeration-driven densification was more pronounced at 600 °C. These results provide fundamental multiscale insights into the structural evolution and carbonation mechanisms of thermo-activated C-S-H, contributing to a better understanding of CO_2 sequestration in cementitious materials.

1. Introduction

In the cement and concrete industry, "carbonation" refers to the interaction between atmospheric CO_2 and either Portland cement clinker or the constituent solids of cement pastes. Carbonation has traditionally been considered detrimental to reinforced concrete structures because it can promote reinforcement corrosion (Sevelsted and Skibsted, 2015a; Sagar and Sharma, 2025). However, in recent years, this conventional view has been reconsidered because the same carbonation reaction has also been recognized as a promising pathway for permanent CO_2 mineralization and the development of sustainable binder systems through capture, storage, and utilization of CO_2 (CCUS) technologies (Ahmed et al., 2024; Seifu et al., 2025). Furthermore, to preserve natural resources and reduce the energy consumption associated with the mining and grinding of carbonatable minerals, CO_2 mineralization has been increasingly conducted using alkaline solid wastes, such as steel slag, coal fly ash, and concrete waste, instead of natural raw minerals (Pan et al., 2020). Against this background, concrete waste is a relevant resource owing to the presence of calcium-bearing phases that readily react with CO_2.

In current recycling practices, most concrete waste—despite its potential for CO_2 mineralization—is predominantly processed into coarse fragments larger than 5 mm, which are referred to as recycled coarse aggregates (RCAs) (Poon et al., 2023; Yu et al., 2026; Mardani et al., 2024; Truong et al., 2025). As interest in RCA recycling continues to grow, attention has also expanded to the re-utilization of concrete waste ground into fine fragments, referred to as recycled cement paste powders (RCPs), which accounts for approximately 40%–50% of the total

* Corresponding author.
E-mail address: sbae@hanyang.ac.kr (S. Bae).

https://doi.org/10.1016/j.dibe.2026.101049
Received 18 June 2026; Received in revised form 2 September 2026; Accepted 13 September 2026
Available online 15 September 2026
2666-1659/© 2026 The Authors. Published by Elsevier Ltd. This is an open access article under the CC BY-NC-ND license (http://creativecommons.org/licenses/by-nc-nd/4.0/).

concrete waste (Huang et al., 2025; Wu et al., 2024). As reported in previous studies, CO_2 can diffuse into the pore structure of hardened cement pastes and form carbonic acid (Jiang et al., 2023; Zajac et al., 2020a; Mao et al., 2024), which subsequently reacts with calcium ions released from $Ca(OH)_2$ and calcium silicate hydrate (C-S-H) to produce $CaCO_3$ and silica-rich phases (Mao et al., 2024; Zheng et al., 2024).

Various carbonation methods, including direct dry, semi-dry, and aqueous carbonation, have been developed (Ahmed et al., 2024; Ali et al., 2026; Seifu et al., 2025; Han et al., 2026). Aqueous carbonation is particularly advantageous because it can mitigate inherent limitations of dry carbonation, such as slow reaction kinetics, the stringent control of pressure and humidity required during this process, and the difficulty in achieving complete carbonation of RCPs (Zajac et al., 2020a, 2023; Mao et al., 2023). Moreover, aqueous carbonation offers the possibility of regulating the polymorphs of $CaCO_3$ formed within carbonated RCPs, which may contribute to improved mechanical performance when used as SCMs (Zajac et al., 2023). Zajac et al., 2020a, 2020b reported that dissolved CO_2 first reacts preferentially with $Ca(OH)_2$ under aqueous carbonation conditions. Once this $Ca(OH)_2$ is consumed, the decalcification of other hydrates, particularly C-S-H, progressively proceeds. During the carbonation process, calcium ions are gradually released from C-S-H and subsequently precipitates as $CaCO_3$, while the silicate framework reorganizes into increasingly polymerized silica phases (Liu et al., 2022a).

In cementitious systems, carbonation often occurs in alkaline environments, either due to the intrinsically high pH of cement pore solutions or through the introduction of alkaline conditions during the carbonation process to enhance CO_2 and calcite solubility (Feng et al., 2026; Zajac et al., 2021a). In alkaline solutions, the presence of alkalis can accelerate the initial stage of carbonation, whereas the reaction kinetics at later stages may be retarded or remain largely unaffected (Zajac et al., 2021a, 2021b). Although the early-stage carbonation behavior of C-S-H under non-alkaline aqueous conditions has been investigated, where dissolved CO_2 promotes the formation of amorphous calcium carbonate (ACC) (Li et al., 2025), the corresponding behavior under alkaline conditions remains poorly understood, despite its practical relevance to aqueous carbonation processes.

In addition to CO_2-sequestration approaches for recycling concrete waste, thermo-activation has been proposed as a complementary method to remove adhered old mortar from RCAs, thereby mitigating the loss of mechanical performance in recycled concrete (Wu et al., 2024). Moreover, thermo-activation has been recognized for its ability to restore the hydraulic reactivity of cementitious materials, providing a promising strategy for producing new hydraulic binders at substantially lower temperatures (500–800 °C) than conventional clinker sintering (>1450 °C) (Abidar et al., 2023; Shui et al., 2008; Li et al., 2018). Numerous studies have demonstrated that such strength recovery arises not only from the remaining unhydrated clinker particles but also from the thermo-activation-induced phase transformations, including the decomposition of C-S-H and the temperature-dependent formation of α-C_2S, β-C_2S, and γ-C_2S (Abidar et al., 2023). In line with these observations, Suh et al., 2020, 2022, 2024a reported that cement pastes heated to 500 °C exhibited mechanical recovery upon rehydration, which was attributed to an increased degree of silicate polymerization in C-S-H. However, although rehydration restores the hydraulicity of dehydrated cement pastes, the resulting properties markedly differ from those of ordinary Portland cement. Higher dehydration temperatures increase the Blaine surface area and promote the formation of reactive phases such as free CaO and ettringite, resulting in greater water demand and shorter setting time (Shui et al., 2009; Semugaza et al., 2023). Consequently, previous research has indicated that incorporating thermo-activated RCPs as supplementary cementitious materials can deteriorate both the mechanical behavior and volumetric stability of cement pastes (Zhai et al., 2025). To address the associated challenges in workability and drying shrinkage, combined approaches have been investigated, such as incorporating fly ash or silica fume, or employing the alkali-activation of thermo-activated RCPs (Zhai et al., 2025; Bogas et al., 2019; Xi et al., 2024). Beyond these approaches, thermo-activated RCPs contain amorphous calcium silicates that readily react with CO_2, making aqueous carbonation a promising strategy for simultaneously enhancing CO_2 uptake and valorizing thermo-activated concrete waste (Xie et al., 2026).

Accordingly, a fundamental understanding of the carbonation behavior of thermo-activated RCPs requires elucidating the intrinsic carbonation behavior of thermo-activated C-S-H, as C-S-H is the primary binding phase in hydrated cement paste and the precursor to the dominant amorphous calcium silicate phase in thermo-activated RCPs (Im et al., 2025; Wang et al., 2018). Previous studies have investigated the intrinsic carbonation behavior of synthetic pure C-S-H, including the effects of Ca/Si ratio (Liu et al., 2022a) and the incorporation of other ions (e.g., Al and Mg) (Li et al., 2019; Liu et al., 2022b). However, the effect of thermo-activation temperatures on the subsequent carbonation behavior of pure C-S-H remains poorly understood. Therefore, this study aims to elucidate the early-age carbonation-induced structural evolution of thermo-activated synthetic C-S-H subjected to different activation temperatures, corresponding to the dehydration (105 °C), decomposition (400 °C), and recrystallization (600 °C) stages.

To this end, synthetic C-S-H was thermo-activated at 105, 400, and 600 °C and subsequently subjected to aqueous carbonation in an initially alkaline condition. A carbonation duration of 30 min was selected to focus on the early-stage carbonation response and to investigate the relative susceptibility of different thermo-activated phases to carbonation. Upon thermo-activation, the intrinsically amorphous C-S-H undergoes progressive structural transformations, involving the transformation of decomposed C-S-H and glass wollastonite phases, followed by the crystallization of wollastonite at elevated temperatures (Ma et al., 2025; Im et al., 2021). Characterizing the carbonation behavior of these amorphous and poorly crystalline phases, particularly during the early-stages of carbonation remains challenging using conventional laboratory-based techniques because of the limited sensitivity of powder X-ray diffraction (XRD) to short-range structural changes, the potential for laser-induced sample alteration or damage during Raman spectroscopy, and the extensive sample preparation and electron-beam induced damage associated with electron microscopy techniques such as scanning and transmission electron microscopy (SEM and TEM, respectively) (Aranda et al., 2026). To overcome these limitations, synchrotron-based X-ray techniques were employed to enable high-resolution, multiscale characterization of the structural and morphological evolution of thermo-activated C-S-H during early-age carbonation. Specifically, synchrotron-based wide- and small-angle X-ray scattering (WAXS and SAXS, respectively), combined with pair distribution function (PDF) and fractal analyses, were employed to probe structural evolution from the atomic to nanoscale levels, while X-ray nanoimaging (XNI) was used to visualize carbonation-induced morphological changes at high spatial resolution.

2. Experimental

2.1. Synthesis of C-S-H pastes and heating procedure

To isolate the intrinsic carbonation behavior of C-S-H from the influence of other cementitious phases, synthetic C-S-H pastes were employed as a model system in this study. Cuboid C-S-H pastes, with dimensions of $5 \times 5 \times 10\ mm^3$ and a target Ca/Si molar ratio of 1.0, were synthesized by mixing $Ca(OH)_2$ (Sigma Aldrich, USA), silica gel (Sigma Aldrich, USA), and distilled water (Im et al., 2023). The hardened C-S-H pastes were stored in a humidity chamber for 28 d; subsequently, they were enclosed in a vacuum-sealed bag for 80 d to prevent carbonation. The morphology and Ca/Si ratio of 0.93 were confirmed using transmission electron microscopy (TEM; JEOL, JEM-2100 F, Japan) combined with energy-dispersive spectroscopy (EDS), as shown in Fig. 1. The purity of C-S-H pastes without other phases, was assessed

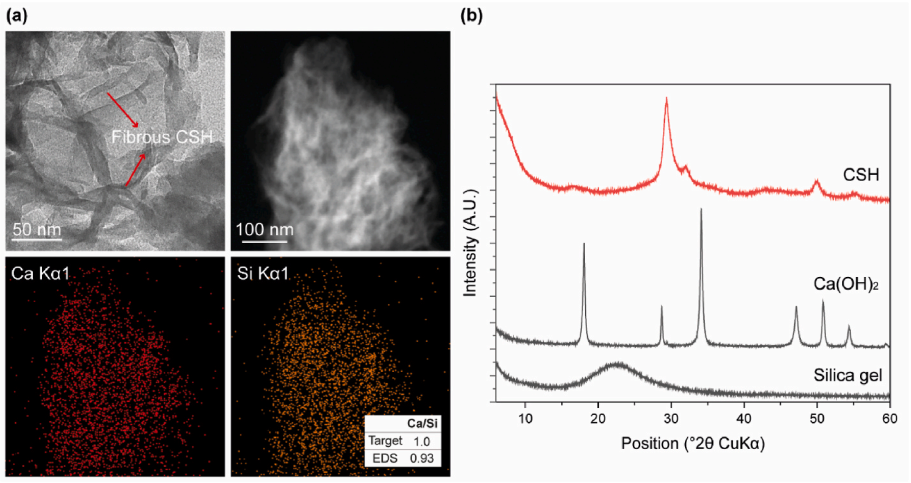

Fig. 1. (a) TEM images of synthesized C-S-H with corresponding Ca and Si elemental mappings. (b) XRD pattern of the raw materials and synthesized C-S-H.

using a powder XRD (D2 Phaser, X-ray source: Cu Kα, wavelength = 1.54 Å, Bruker, Germany) as shown in Fig. 1(b).

Before thermo-activation, the $5 \times 5 \times 10\,mm^3$ C-S-H pastes were sectioned into 1 mm-thick slices. These slices were subsequently subjected to thermo-activation in an electric furnace (LHL-02/17, Nabertherm, Germany) at a controlled heating rate of 10 °C/min, from ambient temperature to the designated activation temperature (T_m), followed by isothermal holding for 2 h (Her et al., 2024). T_m was set to 105, 400, and 600 °C, corresponding to the dehydration, decomposition, and recrystallization stages of C-S-H with a Ca/Si ratio of 1.0, respectively (Im et al., 2021).

2.2. Early-age aqueous carbonation process

Aqueous carbonation was conducted in a reactor equipped with a gas-dosing system, as schematically illustrated in Fig. 2. The experiments were performed at 20 ± 2 °C. A constant gas mixture comprising 90 vol% N_2 (>99.9% purity) and 10 vol% CO_2 (>99.9% purity) was bubbled into 500 mL of 0.1 M NaOH solution at a rate of 0.2 L/min (Zajac et al., 2020a, 2021a). The magnetic stirring speed was set at 200 rpm to achieve a uniform distribution of fine gas bubbles. Prior to the carbonation experiments with C-S-H pastes, a blank test was conducted under same carbonation conditions, and no visible solid precipitation was observed. For the carbonation experiments, bulk C-S-H paste specimens with a thickness of approximately 1 mm were held in the NaOH solution using a mesh holder (Fig. 2(a)). Throughout the CO_2 injection process, the pH of the solution was monitored using a SevenCompact S2220 system (Mettler Toledo, USA) (Fig. 2(a)). As shown in Fig. 2(b), the pH of the solution was stabilized at approximately 6 after 30 min of carbonation. Therefore, to capture early-stage carbonation behavior and to evaluate the influence of the initial alkaline solution, which is expected to be more pronounced during the initial carbonation stage than at later stages, the aqueous carbonation duration was limited to 30 min (Zajac et al., 2021a). This relatively short reaction time also minimizes the potential influence of Na^+ adsorption on the C-S-H structure (Barzgar et al., 2020). After carbonation, the samples were vacuum-dried in a desiccator at −0.08 MPa for 24 h at room temperature before WAXS, SAXS, and XNI analyses (Fig. 2(c)). The carbonated samples were compared with those soaked in the NaOH solution without CO_2 for 30 min.

For clarity, the samples are denoted as T20, T105, T400, and T600 for C-S-H pastes thermally activated at 20, 105, 400, and 600 °C, respectively, which were immersed in a NaOH solution for 30 min without CO_2 exposure. The suffix "-C" (e.g., T20-C) indicates specimens subjected to 30 min of aqueous carbonation under the conditions described above.

2.3. Multiscale morphological analysis of thermo-activated C-S-H pastes after aqueous carbonation

To investigate the phase assemblage and microstructural evolution of the thermo-activated C-S-H pastes after wet carbonation, synchrotron-based WAXS, SAXS, and XNI experiments were conducted. First, WAXS experiments were used to explore the changes in the lattice structure and interatomic distance of the C-S-H phase across a length-scale below 35 Å. Second, SAXS experiments were conducted to investigate the C-S-H structure across a length-scale ranging from 102 to 104 nm. These analyses considered the multiscale structure, including interlayers, gel pores, inner (dense; I_P C-S-H) and outer (less dense; O_P C-S-H) C-S-H phases, and air voids, as illustrated in Fig. 2(c) (Kunther et al., 2017).

2.3.1. WAXS analysis

To determine the lattice structure and local atomic arrangement of thermo-activated C-S-H pastes after aqueous carbonation, and account for the highly amorphous nature of the decomposed C-S-H phase, PDF (*G(r)*) analyses were conducted using high-energy WAXS (X-ray energy: 69.8 keV, λ = 0.178 Å; BL22XU, SPring-8) (Im et al., 2023; Bae et al., 2018). The high-resolution WAXS patterns and PDFs provide reciprocal- and real-spatial information regarding interatomic distances, enabling the evaluation of nanostructural changes at length scales below 35 Å induced by thermo-activation and subsequent carbonation. The normalized total scattering data were produced in PDFgetX3 with $Q_{max} = 18\,Å^{-1}$, which was selected to minimize the truncation oscillation errors in the long-range order region above 20 Å, and the probability function (*G(r)*) was obtained via Fourier transformation using Eq. (1) (Kim et al., 2022a).

$$G(r) = 4\pi r[\rho(r) - \rho_0] = \frac{2}{\pi}\int_{Q_{min}}^{Q_{max}} Q[S(Q) - 1]\sin(Qr)dQ \quad (1)$$

Here, *S(Q)* denotes the scattering structure factor, and $\rho(r)$ represents the local atomic number density at an interatomic distance (*r*).

Furthermore, the WAXS patterns were analyzed using Rietveld refinement to quantify the phase composition of the thermo-activated C-S-H pastes before and after carbonation. In this study, because the synchrotron WAXS measurements were conducted on bulk pastes to characterize the intact internal matrix, incorporating an internal standard for Rietveld analysis was not feasible (Zajac et al., 2020a).

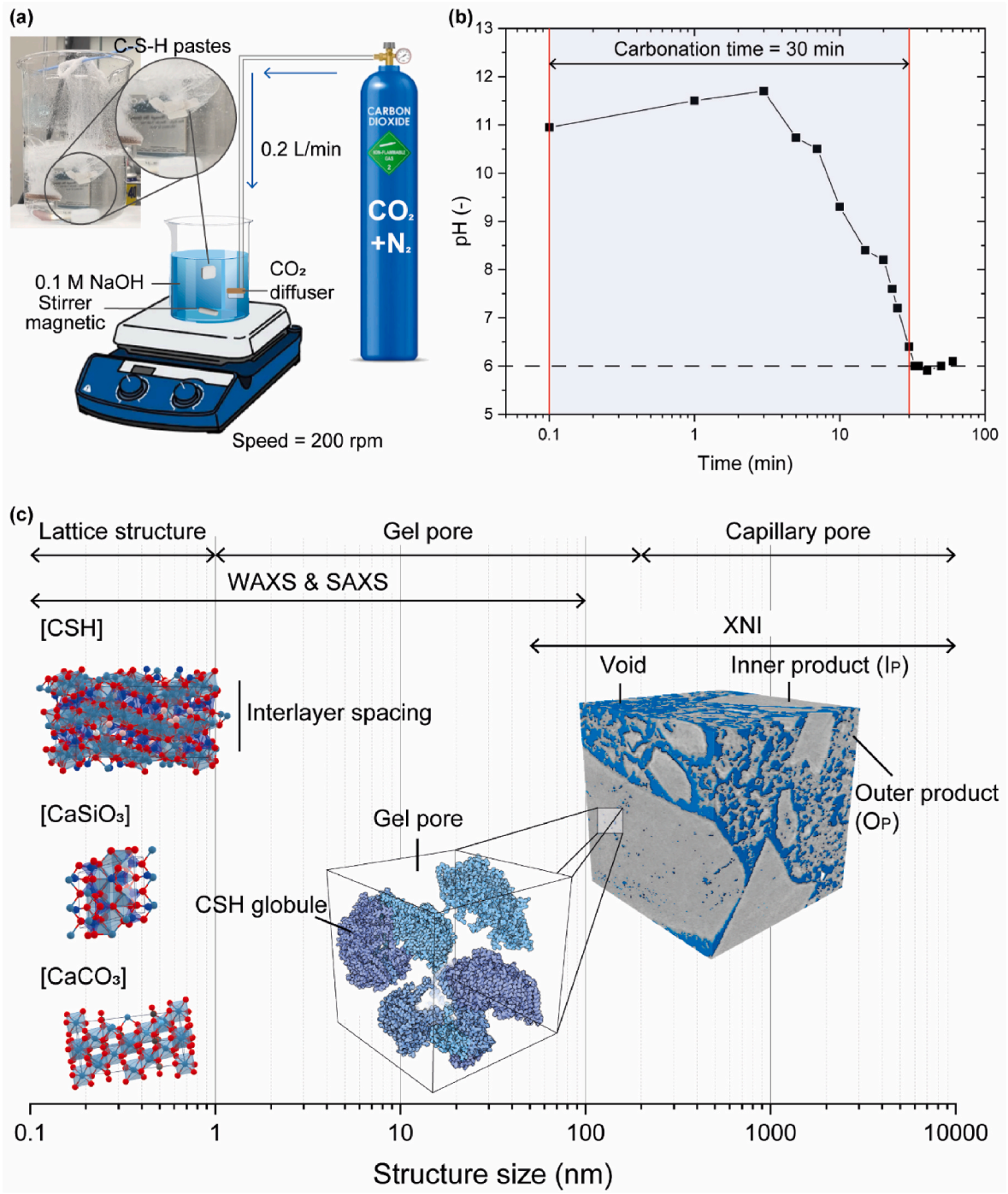

Fig. 2. (a) Schematic representation of the wet carbonation process and (b) pH evolution during the wet carbonation experiment. The square symbols indicate the sampling points. (c) Schematic diagram of the multiscale structure of C-S-H probed by WAXS/SAXS and XNI.

Accordingly, the poorly crystalline C-S-H fraction was quantified using a Pawley fit model within the partial or no known crystal structure (PONKCS) approach (Bae et al., 2018, 2020; Her et al., 2021; Naber et al., 2019; Li and Scrivener, 2025). The Pawley fit model for C-S-H was constructed based on the structure of 11 Å tobermorite (F2dd space group, COD 9005497), with initial unit-cell parameters of $a = 11.25$ Å, $b = 7.2$ Å, $c = 56.8$ Å (Bae et al., 2020). The structural models of β-wollastonite (COD 9011452) and calcite (COD 1547350) were included in the Rietveld refinement based on their identification in the WAXS patterns. The quality of the Rietveld refinement was evaluated using the weighted-profile residual (R_{wp}), calculated according to Eq. (2):

$$R_{wp} = \left(\frac{\sum_i w_i \left(y_{i,obs} - y_{i,calc} \right)^2}{\sum_i w_i \left(y_{i,obs} \right)^2} \right)^{1/2} \quad (2)$$

where w_i, $y_{i,obs}$, and $y_{i,calc}$ denote the quantities of the ith phase, the experimentally observed X-ray scattering intensity, and calculated intensities of ith phase, respectively.

The PDF data were further analyzed using PDFgui to investigate the local atomic structure of C-S-H. Based on the experimental data, Q_{max} was set to 18 Å^{-1}, while Q_{damp}, accounting for the damping of the experimental PDF signal due to the limited Q-range, was fixed at

0.05 Å^{-1}. The temperature parameter for each PDF fitting was set according to the corresponding thermo-activation temperature. The structural models of C-S-H (COD 9005497), β-wollastonite (COD 9011452), calcite (COD 1547350), and vaterite (COD 1508970) were included in the PDF fitting. During the refinement, the atomic-site parameters were fixed. PDF fitting was performed over an r-range of 1.2–8 Å, and the quality of the fits was evaluated using the weighted residual factor (R_w), as expressed in Eq. (3) (Im et al., 2021).

$$R_w = \frac{\sum_{i=1}^{N} w(r_i)[G_{obs}(r_i) - G_{cal}(r_i)]^2}{\sum_{i=1}^{N} w(r_i)[G_{obs}(r_i)]^2} \quad (3)$$

where $w(r_i)$, $G_{obs}(r_i)$, and $G_{cal}(r_i)$ indicate the weighting factor at ri, the observed experimental PDF, and the calculated PDF, respectively. A Smaller R_w value represents better agreement for PDF refinement (Im et al., 2021).

2.3.2. SAXS analysis

SAXS experiments using synchrotron radiation were conducted at the 4C beamline of the Pohang Light Source-II (PLS-II), a third-generation storage-ring facility located at the Pohang Accelerator Laboratory (PAL; Republic of Korea). The storage ring operated at 3.0 GeV with a beam current of 400 mA under top-up conditions, and a monochromatic X-ray beam with a wavelength of 0.7337 Å was utilized for data acquisition (Im et al., 2025; Kim et al., 2017, 2020, 2022b). Scattering data were collected using a Rayonix 2D SX165 detector (Evanston, USA) featuring a pixel size of 7.96 × 7.96 μm^2. As shown in Fig. 3 (A), the sample-to-detector distance (SDD) was 5 m for SAXS, 0.2 m for WAXS, and 1 m for merging SAXS and WAXS data. The scattering angles calibration was carried out using Ti-SBA-15 (Sigma Aldrich, USA). The resulting 2D scattering images were azimuthally averaged to obtain scattering intensity as a function of the momentum transfer vector, Q ($Q = 4\pi \cdot \sin\theta/\lambda$). Data acquisition times of 1, 0.5, and 10 s were applied at sample-to-detector distances (SDDs) of 5, 1, and 0.2 m, respectively, yielding an effective Q range of 0.005–2.7 Å^{-1}, while avoiding radiation-induced damage to the samples. The background data (empty sample holder) were subtracted, and datasets collected at different SDDs were merged using the PRIMUS package in ATSAS software (Cho et al., 2023).

Algebraic decay behavior is commonly observed in SAXS experiments on hydrated cement and C-S-H, as illustrated in Fig. 3(b) (Im et al., 2025; Maruyama et al., 2017). The scattering intensity profile, plotted as log $I(Q)$ vs. log Q, exhibits a power-law relationship, $I(Q) = Q^{-\alpha}$, where α is the slope, indicating the fractal characteristics of the C-S-H phase (Trapote-Barreira et al., 2015). For $2 < \alpha < 3$, the structure is typically associated with "volume fractal systems," where the volume fractal dimension $D_V = \alpha$. Conversely, for $3 < \alpha < 4$, the structure is generally associated with "surface fractal systems," and the surface fractal dimension is given by $D_S = 6 - \alpha$. At $\alpha = 4$, the SAXS profile suggests the Porod regime, corresponding to a smooth surface. The SAXS profiles of the C-S-H phase exhibited two distinct slope regimes, justifying the application of the analytical model based on scale separation. The low-Q region (0.005–0.1 Å^{-1}) was attributed to fractal scattering, whereas the high-Q region (0.1–0.3 Å^{-1}) was governed by Porod behavior. Notably, the slope did not exceed 3, indicating that the profiles were governed solely by a volume-fractal regime for the parameter estimation. The parameters obtained from Eq. (4) include the volume fractal dimension (D_V), volume fraction of C-S-H particles (Φ), correlation length (ξ_V), and radius of C-S-H building blocks (R_O).

$$I(Q) = I_v(Q) + BGD = \varnothing V_p |\Delta\rho|^2 \left\{ \frac{\eta R_O^3}{\beta R_0^3} \left(\frac{\xi_v}{R_O} \right)^{D_v} \times \frac{\sin[(D_v - 1)\arctan(Q\xi_v)]}{(D_v - 1)Q\xi_v \left[1 + (Q\xi_v)^2\right]^{\frac{(D_V-1)}{2}}} + (1 - \eta)^2 \right\} F^2(Q) + BGD, \quad (4)$$

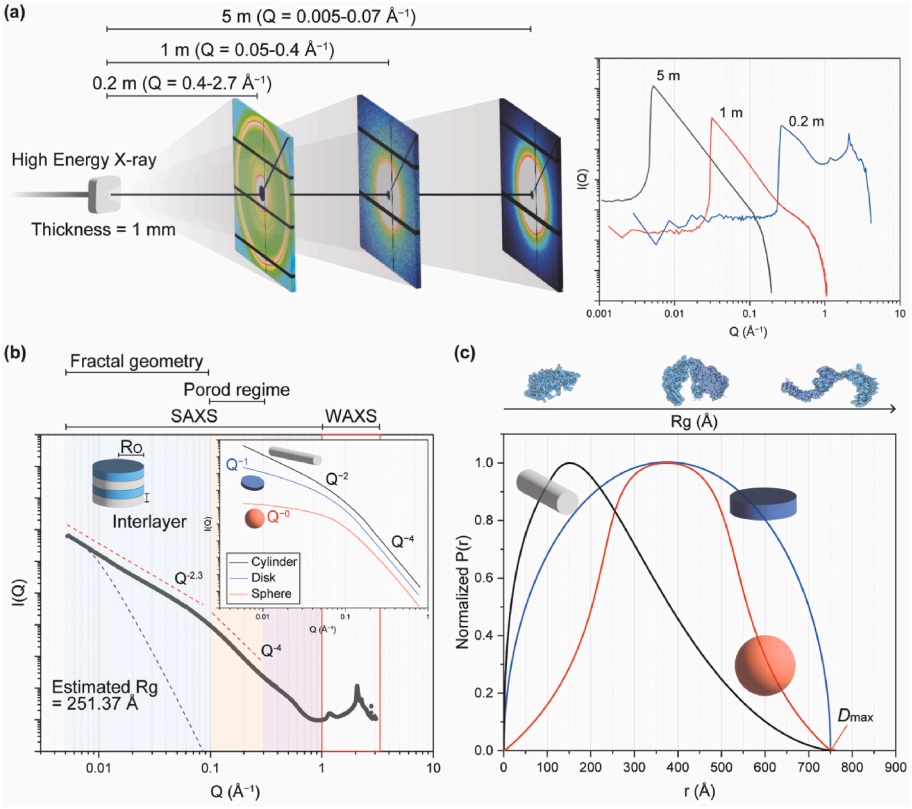

Fig. 3. Schematic illustration of (a) SAXS experiments with (b) indication of the fractal disc and Porod regions. (c) PDDFs indicative of particle shape.

Here, BGD is defined as the incoherent flat background scattering, and $|\Delta\rho|^2$ denotes scattering contrast factor between pores (i.e., air voids and H_2O) and solid particles (Trapote-Barreira et al., 2015). The corresponding $|\Delta\rho|^2$ values for the C-S-H slices are listed in Table 1. These model parameters were optimized using a least-squares fitting procedure implemented in the Irena package to minimize the difference between the experimental and fitted scattering profiles (Ilavsky and Jemian, 2009).

In addition to the fractal fitting, the pair distance distribution function (PDDF), that is the probability ($P(r)$) as a function of radial distance r from the edge of the interparticle, was determined using Moore functions (indirect Fourier transformation), as described in Eq. (5) (Trapote-Barreira et al., 2015; Moore, 1980). This curve-fitting analysis covers the measured Q-range of 0.005–1.0 $Å^{-1}$. As reported in previous studies (Li et al., 2016), the PDDF has been used to determine the particle shapes (e.g., sphere, rod, and disk), as well as their maximum dimension (D_{max}, the maximum distance from the geometric center) (Hamley, 2021). Fig. 3(c) compares the PDDF for objects with different shapes (Hamley, 2021).

$$P(r) = \frac{1}{2\pi^2}\int_0^{Q_{max}} I(Q)Qrsin(Qr)dQ \tag{5}$$

2.3.3. High-resolution synchrotron X-ray nanoimaging

Synchrotron-based XNI was performed to characterize the morphological features of the C-S-H pastes after carbonation at the 7C Beamline of the PLS-II with a field of view (FOV) of 50 μm and a pixel resolution of 50 nm (Cho et al., 2024; Suh et al., 2024b). XNI measurements were performed only on the T20 and T600 samples to investigate the morphological differences between the non-thermo-activated and thermo-activated C-S-H pastes after carbonation. The beamline uses 9.3 keV X-rays to acquire 720 transmission X-ray microscopy (TXM) projections by rotating the sample in an angle step of 0.25° with each image recorded on a 2048 × 2048 pixel scintillator detector with a binning size of 2 × 2 (Marana, Andor Technology, UK). Octupus 8.1 was used to reconstruct the TXM projections after subtracting the background. To reduce the intrinsic noise of the XNI images, a Gaussian filter with a kernel size of 2 × 2 × 2 voxels and a median filter were applied using Avizo software (Thermo Fisher Scientific, US) (Suh et al., 2024b, 2024c). Finally, a cuboid region with a volume of 20 × 20 × 20 $μm^3$ was extracted from the entire 3D computed tomography (CT) stack. The extracted volume of interest (VOI) for tomographic reconstruction consisted of 400 × 400 × 400 voxels, each with a cubic voxel of 50 × 50 × 50 nm^3. An example of a sliced grayscale image and the grayscale profile along the white line in the image are shown in Fig. 4(a). Based on the grayscale intensities, the I_P C-S-H, O_P C-S-H, and pores can be segmented using histogram deconvolution with a Gaussian distribution (Fig. 4(b and c)) (Bossa et al., 2015; Pae et al., 2024). Furthermore, the fractal dimension (D) of each segmented phase, indicating the complexity of the phase surface, was calculated using the 3D box-counting method in the Avizo software (Wang et al., 2019). The fractal dimension, D, of the 3D solid phases and pores was compared with the volume fractal dimension (D_V) obtained from the SAXS measurements.

Table 1
Calculated scattering contrast factor, $|\Delta\rho|^2$, of C-S-H slices according to the thermo-activated temperature using the measured sample density and the *Irena and Nika* packages in Igor software (Ilavsky and Jemian, 2009).

Activation temperature (°C)	Density (g/cm^3)	$\|\Delta\rho\|^2$ (×10^{20} cm^{-4})
20	1.6	203.4
105	2.3	219.1
400	2.2	273.8
600	2.1	292.3

2.4. Thermogravimetric analysis and Raman spectroscopy

To further investigate the difference in $CaCO_3$ content between the T20-C and T600-C samples, thermogravimetric (TG) analysis was conducted using approximately 20 mg of finely ground powder. The samples were heated from ambient temperature (20 °C) to 1000 °C at a rate of 10 °C/min using a thermogravimetric analyzer (STA 7200, Hitachi, Japan) under an N_2 flow rate of 200 mL/min. The $CaCO_3$ content was determined using Eq. (6) (Cho et al., 2026).

$$W_{CC} = WL_{CC} \times \frac{m_{CaCO_3}}{m_{CO_2}}. \tag{6}$$

where W_{CC} is the $CaCO_3$ content, WL_{CC} is the mass loss attributed to $CaCO_3$ decomposition, determined by integrating the derivative thermogravimetric (DTG) peaks in the temperature range of 500–800 °C, and m_{CaCO_3} and m_{CO_2} are the molecular masses of $CaCO_3$ and CO_2, respectively (Cho et al., 2026).

In addition, Raman spectroscopy was performed using a Ramanwalk (Bruker, Germany) equipped with a 532 nm excitation laser. The laser was focused on the sample using a 20× objective lens (NA = 0.45) at a power of approximately 30 mW. Raman spectra were collected using a 600 grooves/mm grating with an exposure time of 1 s.

3. Results and discussion

3.1. Changes in the reciprocal- and real-space of thermo-activated C-S-H after aqueous carbonation

Fig. 5 depicts the high-energy X-ray scattering patterns of thermo-activated C-S-H before and after aqueous carbonation at activation temperatures of 20, 105, 400, and 600 °C. At all activation temperatures, carbonation induced distinct changes in the primary C-S-H peak at $Q = 2.1$ $Å^{-1}$, which is assigned to the CaO layer corresponding to the (020) plane (Wang et al., 2026). Due to the short carbonation duration (30 min), calcite reflections were detected only at significantly low intensities. At the dehydration stage of C-S-H activated at 105 °C, the main C-S-H peak became appreciably narrower after carbonation (Fig. 5(b)) compared with that of the non-activated C-S-H (Fig. 5(a)), suggesting that dehydration facilitated structural rearrangement during carbonation by promoting Ca dissolution and subsequent calcite formation (Liu et al., 2022a). In addition, the peak intensity of the (020) plane increased after carbonation in the T105 samples, whereas the T20 and T20-C samples exhibited negligible changes. Cai et al. (2026) reported that the early stage of carbonation is characterized by a pronounced decalcification of the C-S-H interlayer. These results indicated that the loosely packed interlayer structure, resulting from the evaporation of moisture after activation at 105 °C, facilitates an increased degree of structural order and accelerates calcite formation (Im et al., 2025).

After carbonation of T400 samples, the peak intensity of β-wollastonite decreased, while the calcite reflections increased, as shown in Fig. 5(c). Furthermore, the T600-C samples exhibited the most pronounced increase in the calcite peak intensity at $Q = 2.05$ $Å^{-1}$ among other C-S-H pastes activated at lower temperatures (Fig. 5(d)). In the Q region above 2.5 $Å^{-1}$, the peak intensity decreased after carbonation for T20, T105, and T400, whereas an opposite trend was observed for the T600-C samples. Consequently, these observations suggest that carbonation enhances the structural disorder of C-S-H activated at the dehydration and decomposition stages, thereby leading to the decomposition of C-S-H and the glass β-wollastonite (Im et al., 2025). In addition, the extent of calcite formation progressively increased at higher activation temperatures, as evidenced by the quantitative results summarized in Table 2.

The detailed quantification results for the thermo-activated C-S-H pastes before and after carbonation, obtained from the Rietveld refinement of the high-energy X-ray scattering patterns are listed in Table 2,

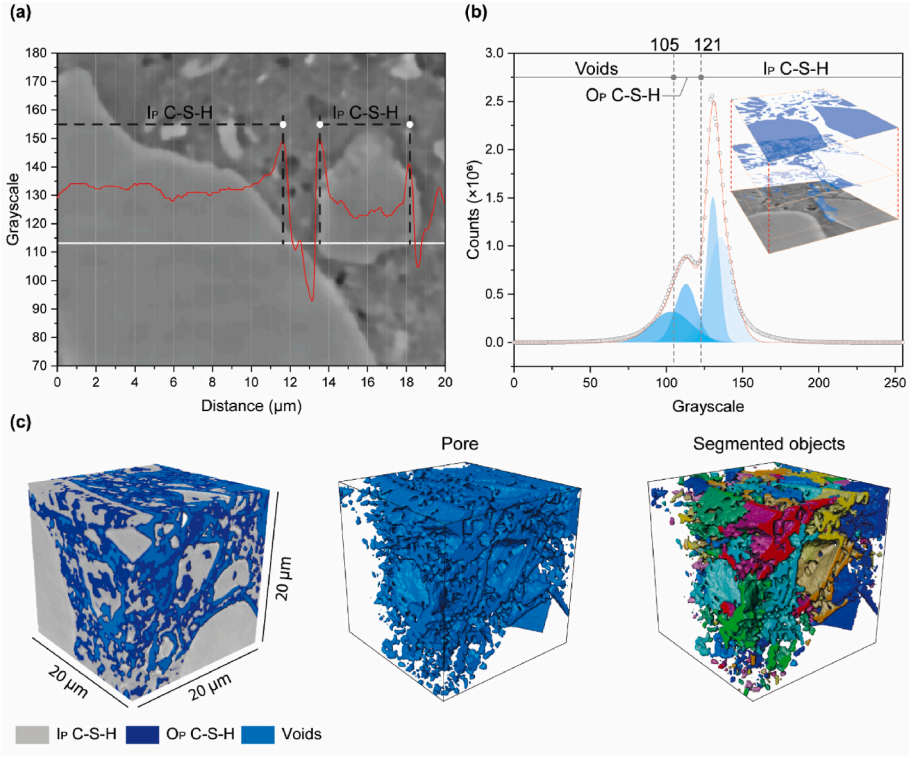

Fig. 4. (a) Sliced grayscale image and line probe analysis results, (b) thresholding method applied to the VOI for voids and solid phase segmentation using Gaussian functions, and (c) separation and segmentation of 3D pore objects.

and the corresponding refined patterns are shown in Fig. S1. Upon carbonation, the C-S-H fraction decreased markedly in T400 (12.4%) than in those activated at 600 °C (9.8%). By contrast, β-wollastonite showed the opposite trend, decreasing slightly at 400 °C (3.7%) but much more prominently at 600 °C (11.9%). These results suggest that the relative contribution of C-S-H and β-wollastonite to carbonation varies with thermo-activation temperature, with a greater consumption of β-wollastonite observed at T600 compared to T400. To further evaluate the carbonation extent and support interpretation, additional TG and Raman analyses were performed on T20, T20-C, T600, and T600-C, as discussed in Section 3.4.

To further investigate the temperature-dependent phase reactivity during carbonation, the changes in the interatomic distances were analyzed using PDF. The enlarged view of the PDF curves, isolating the *r*-range from 1 to 5 Å, extracted from the whole PDF profiles spanning 0–50 Å (Fig. S2), are shown in Fig. 6. Due to the initial carbonation stage with short reaction time of 30 min, the variation in the damping region, as well as the peak evolution beyond 30 Å, were negligible. Conversely, the short-range atomic correlations within the *r*-range of 1–5 Å exhibited discernible, temperature-dependent changes upon carbonation, reflecting modifications in the local atomic structure, as highlighted in Fig. 6.

Notably, the first Si–O (~1.6 Å) and Ca–O (~2.4 Å) correlations exhibited contrasting trends before and after carbonation as a function of the thermo-activation temperature. For the Si–O correlations, carbonation led to an increase in peak intensity in the T20 samples, whereas a slight change was observed at 105 °C. By contrast, a progressive decrease in peak intensity was evident at higher activation temperatures at 400 and 600 °C. On the other hand, the Ca–O correlations exhibited an opposite trend, with increased peak intensity in the T20 sample and reduced intensity of 400 °C upon carbonation. These results suggest that thermo-activation induced distortion of the local Ca–O environment may facilitate Ca^{2+} leaching and enhance carbonation reactivity (Zheng et al., 2021). Such an effect has also been reported for wollastonite polymorphs, in which distorted Ca–O coordination was associated with enhanced carbonation reactivity (Liu et al., 2021).

As a result, the Ca/Si ratios of the T20 and T105 samples remained constant before and after carbonation. For the C-S-H pastes thermo-activated at 400 °C, the Ca/Si ratios reduced by CaO precipitation during thermo-activation were restored to their initial value after carbonation (Zheng et al., 2021). Although the Ca/Si ratios of T600 exhibited minimal changes relative to those of T400, a slight increase after carbonation was observed from the value reduced by CaO precipitation. In addition, across all samples, the intensities of Si–Si (~3.1 Å), Si–O (~4.2 Å) peaks increased after carbonation, suggesting the development of a more polymerized silicate structure (Liu et al., 2022a; Morandeau and White, 2015).

Fig. 7 compares the carbonation-induced structural changes in the T20 and T600 samples using their PDF difference ($\Delta G(r)$) profiles. As presented in Fig. 7(a), the magnitude of $\Delta G(r)$ is substantially larger for T600 than for T20, indicating more extensive structural rearrangement upon carbonation. In the short-range region (0–5 Å), comparable changes were observed for T20 and T600. Previous studies have shown that C-S-H and wollastonite carbonation induced local structural rearrangement associated with decalcification and the formation of amorphous silica (Morandeau and White, 2015; Wang et al., 2025). Therefore, the changes observed in this region may include contributions from newly formed amorphous silica and poorly ordered $CaCO_3$ (e.g. ACC). In contrast, $\Delta G(r)$ of T600 exhibited a substantially larger amplitude than that of T20 in the 5–30 Å range. Thermo-activation disrupts the medium-to long-range structural ordering of C-S-H through the formation of crystalline carbonated phases, such as calcite. The larger $\Delta G(r)$ of T600 in this range may thus reflect pronounced structural reorganization of the thermoactivated phases together with the development of medium-to long-range ordering associated with crystalline carbonation formation, which is further evaluated by TG

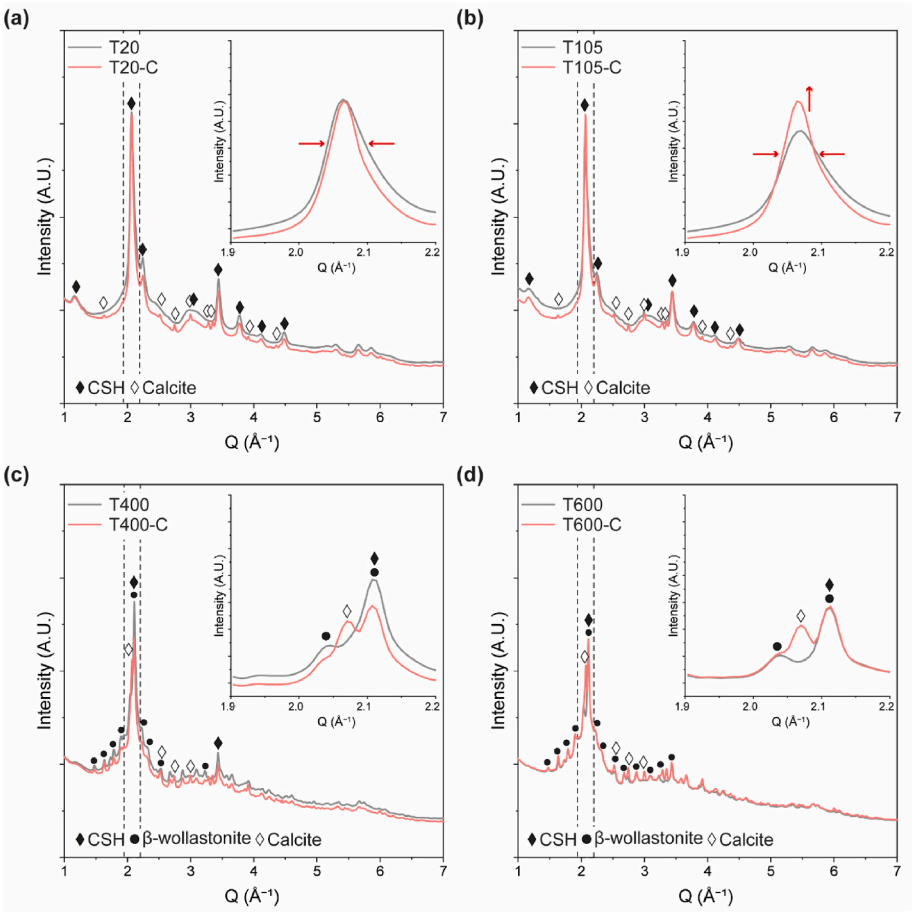

Fig. 5. Synchrotron X-ray scattering patterns (Q = 1–7 Å^{-1}) of (a) T20 and T20-C; (b) T105 and T105-C; (c) T400 and T400-C; and (d) T600 and T600-C.

Table 2
Phase composition of thermo-activated C-S-H pastes before and after carbonation determined by Rietveld refinement.

Label	Phase content (wt.%)			R_{wp}
	C-S-H	Wollastonite	Calcite	
T20	100	-	-	3.3
T20-C	87.8	-	12.2	1.7
T105	100	-	-	2.3
T105-C	85.1	-	14.9	3.2
T400	54.6	45.4	-	2.4
T400-C	42.2	41.7	16.1	2.3
T600	43.9	56.1	-	2.3
T600-C	34.1	44.2	21.7	1.8

Note: R_{wp}, weighted-profile residual; "-" indicates that the corresponding phase was not detected in the WAXS pattern.

analysis in the following section (Fig. 17) (Wang et al., 2025).

Table 3 summarizes the phase compositions of the thermo-activated C-S-H pastes before and after carbonation based on PDFgui refinement within a range between 1.2 and 8 Å, providing a quantitative assessment of the carbonation-induced phase evolution in short-range order (Fig. S3 and Fig. S4). However, PDFgui fitting requires an appropriate structural model for each phase. Consequently, amorphous silica and ACC, for which reliable structural models were unavailable, were not included in the fitting, despite the capability of short-range PDF analysis to characterize the local structure of amorphous material. Their possible contributions to the experimental PDF therefore cannot be completely excluded.

In the PDFgui analysis, calcite and vaterite were used for calculation. The total contributions of $CaCO_3$ phases progressively increased with increasing thermo-activation temperature. In addition, the calcite contribution increased with increasing thermo-activation temperature, consistent with the trend observed in the Rietveld refinement results. After carbonation, the reduction in β-wollastonite was more pronounced than that of C-S-H for the T400 and T600 samples. This result suggests that β-wollastonite exhibits higher reactivity toward carbonation than decomposed C-S-H. Due to the limitation of structural information available for amorphous silica and ACC, $CaCO_3$ formation was further evaluated using TG and Raman analyses.

3.2. *Changes in thermo-activated C-S-H globules after aqueous carbonation at Å–nm scale*

Fig. 8 depicts the SAXS profiles of thermo-activated C-S-H pastes before and after carbonation, measured over a *Q*-range of 0.005–3 Å^{-1}, which captures the structural dimensions of C-S-H globules ranging from approximately 1 to 1250 Å. It should be noted that vacuum drying may induce C-S-H shrinkage and alter the pore structure through the removal of pore water. Nevertheless, since the same drying procedure was applied to all samples, the structural characteristics derived via SAXS allow for consistent relative comparison among the samples.

As the treatment temperature increased beyond 105 °C, the peak observed at 0.6 Å^{-1}, associated with the interlayer spacing of C-S-H ($d \approx 10.5$ Å), disappeared (Im et al., 2025). As presented in Fig. 8(b), the hump observed near $Q = 0.07$ Å^{-1} shifted slightly to the lower *Q* values, indicative of an increase in the solid interparticle distance as the C-S-H phase decomposed after thermo-activation at 600 °C (Hamley, 2021). In addition, the corresponding phase transformations after thermo-activation and carbonation are reflected in the WAXS region, as discussed in Section 3.1.

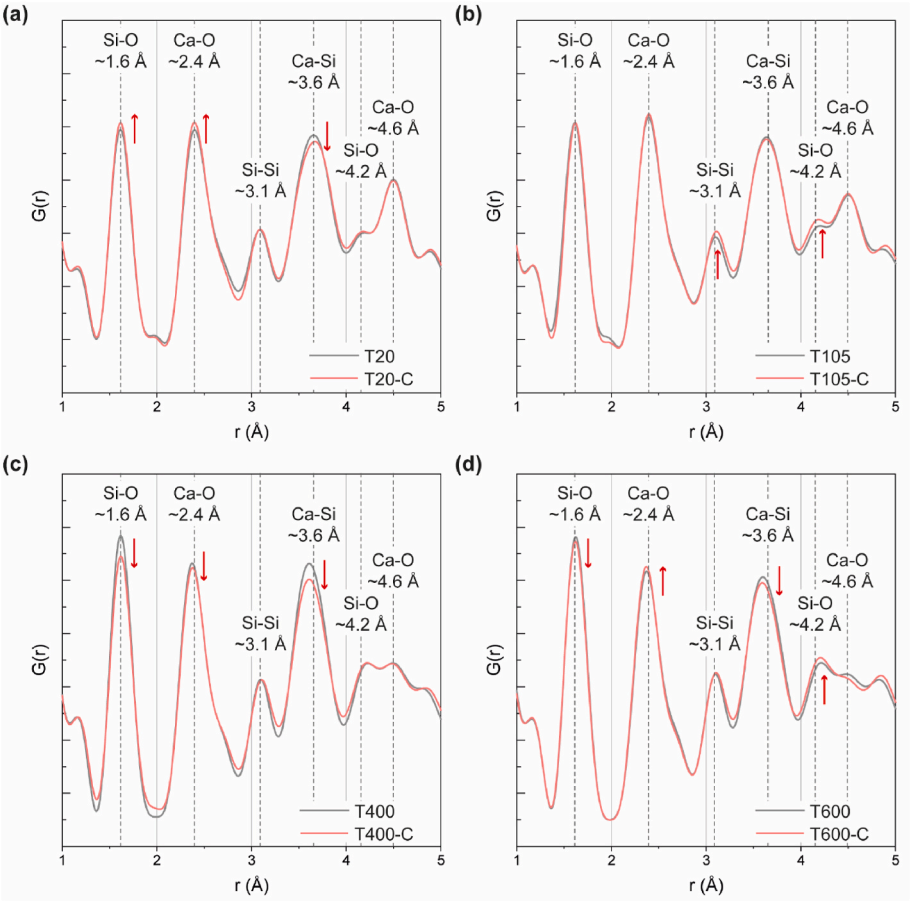

Fig. 6. PDFs in the *r*-range of 1–5 Å for (a) T20 and T20-C, (b) T105 and T105-C, (c) T400 and T400-C, and (d) T600 and T600-C. The labeled atomic pairs indicate the characteristic pair correlations and their corresponding *r*-positions.

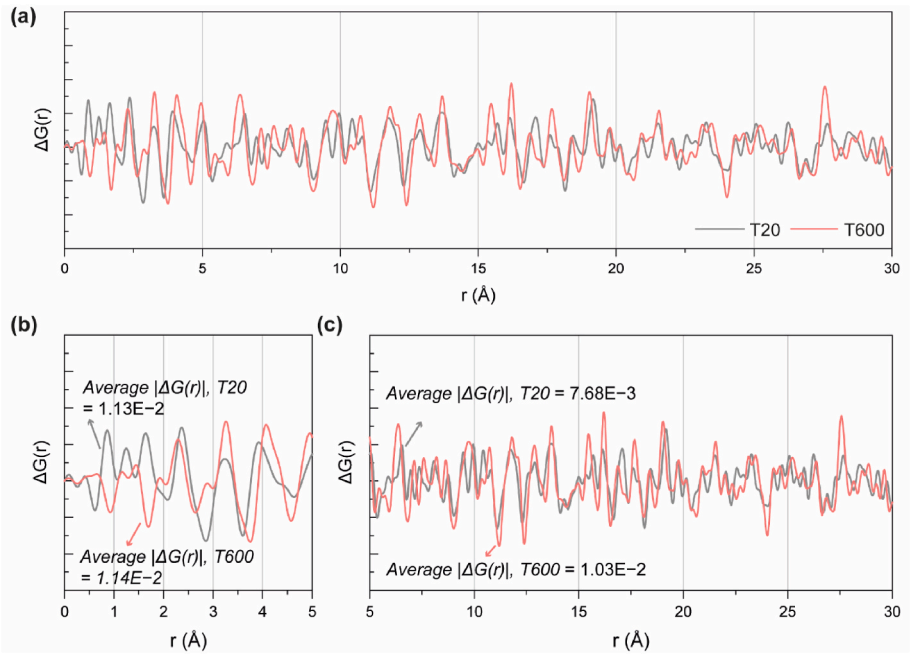

Fig. 7. PDF differences ($\Delta G(r)$) between T20 and T20-C (gray), and between T600 and T600-C (red), in the *r*-range of (a) 0–30 Å; (b) 0–5 Å; and (c) 5–30 Å. The labeled average $|\Delta G(r)|$ values represent the average magnitude of the PDF differences within the corresponding *r*-ranges.

Table 3
Phase composition of thermo-activated C-S-H pastes before and after carbonation determined by PDFgui calculation.

Label	C-S-H (wt.%)	Wollastonite (wt.%)	Calcite (wt.%)	Vaterite (wt.%)	*a* axis (Å)	R_w
T20	100	-	-	-	11.21	0.45
T20-C	79	-	13	8	11.16	0.42
T105	100	-	-	-	11.2	0.45
T105-C	76	-	14	10	11.28	0.43
T400	45	55	-	-	10.89	0.36
T400-C	36	37	15	12	11.04	0.33
T600	28	72	-	-	10.48	0.38
T600-C	22	48	18	12	10.38	0.49

Note: "-" indicates that the corresponding phase was not included in the PDFgui fitting.

Consistent with the WAXS observations in Section 3.1 (Fig. 5), the sharpening of the peak at $Q = 2.1$ Å^{-1} after aqueous carbonation for the T20 and T105 samples is more clearly resolved in the high-Q region of the SAXS profiles (Fig. 8(c)). Notably, the T105-C sample exhibited a more pronounced increase in the intensity of the peak at $Q = 2.1$ Å^{-1} compared with the T20-C sample. As shown in Fig. 8(b), the hump observed in T20 and T105 ($Q = 0.07$ Å^{-1}) was flattened after carbonation, with a more pronounced flattening observed for T105. These results suggest that aqueous carbonation facilitates the diffusion of CO_3^{2-} species into pore spaces generated by the evaporation of free moisture during the dehydration stage at the thermo-activation temperature of 105 °C, thereby promoting calcite formation within the CaO layer and the agglomeration of C-S-H globules (Zheng et al., 2021; Constantinides and Ulm, 2007; Li et al., 2024). At higher activation temperatures (T400 and T600), after aqueous carbonation, the peak associated with β-wollastonite was transformed into $CaCO_3$, accompanied by crystal lattice expansion (Cho et al., 2024; Wang et al., 2024). Furthermore, for the T400 and T600 samples, the hump was retained even after carbonation. Detailed changes in slope of the log–log SAXS plots within the low Q range (0.005–0.1 Å^{-1}) were analyzed using volume fractal fitting.

Fig. 9 shows the power-law decay SAXS profiles in the Q-range of 0.005–0.1 Å^{-1}, along with the fitting results obtained using the fractal model proposed by Allen et al. (Maruyama et al., 2017; Allen et al., 2007; Thomas et al., 2008). The power-law exponent, α, which is related to the fractal dimensions of C-S-H pastes (Bae et al., 2015), was evaluated using a volume fractal model, as all α values were below 3, which is characteristic of a branched and cross-linked 3D network structure (Allen et al., 2007; Kupwade-Patil et al., 2018). Before thermo-activation, the T20-C sample exhibited a steeper slope than T20 (Fig. 9(a)), indicating enhanced structural heterogeneity associated with the formation of crystalline $CaCO_3$ and amorphous silica gel upon carbonation (Nirschl and Guo, 2018). In addition, no apparent change in the SAXS slope was observed for the T105 and T400 samples before and after carbonation, as depicted in Fig. 9(b) and (c), respectively. At the highest thermo-activation at 600 °C (Fig. 9(d)), the scattering profiles exhibited two distinct power-law decay regions, with a slope of approximately 2.1 in the low-Q region ($Q < 0.03$ Å^{-1}; $d > 210$ Å) and 2.9 in the high-Q region ($Q > 0.03$ Å^{-1}; $d < 210$ Å). This result reflects a highly heterogeneous microstructural system resulting from the decomposition of C-S-H and the formation of pyrolyzed products, including β-wollastonite and CaO (Im et al., 2025). After carbonation of T600 (i.e., T600-C), the α value in the low-Q region increased to 2.7, becoming comparable to that in the high Q region ($\alpha = 2.9$). The convergence of α values across different Q regions implies a similar fractal dimension over the broad length scale ranging from 60 to 1250 Å, reflecting uniform structural complexity of the carbonated phases (Maruyama et al., 2017; Chiang et al., 2013).

To further illustrate this trend, the overall variations in the volume fractal dimension D_V as a function of the activation temperature before and after carbonation are shown in Fig. 10(a). Regardless of the thermo-activation temperature, the carbonated samples exhibited higher D_V values than the corresponding samples before carbonation. Based on the mass fractal relationship between the number of particles (N_P) in a cluster, radii of the aggregates (R_O), and D_V, as described in Eq. (4), an increase in the fractal dimension reflects a more compact particle aggregation with a constant aggregate size (Anovitz and Weston, 2020).

$$N_P \propto R_O^{D_V} \tag{4}$$

Accordingly, based on the variations in D_V and R_O shown in Fig. 10 (a) and (b), respectively, distinct carbonation behaviors were identified between the T20 and thermo-activated samples. For the T20 samples, the number of particles increased while R_O decreased from 30 to 15 Å (Fig. 10(b)) due to the shrinkage of C-S-H globules induced by the dissolution of Ca^{2+} and OH^- upon carbonation (Chiang et al., 2014). This reduction in R_O is associated with a shortened ξ_V (Fig. 10(c)), indicating the disruption of interparticle interactions and a concomitant decrease in the volume fraction of solids (Fig. 10(d)) (Chiang et al., 2014). In line with previous studies, carbonation C-S-H involves initial decalcification and silicate-chain polymerization, followed by the formation of $CaCO_3$ and amorphous silica (Liu et al., 2022a; Sevelsted and Skibsted, 2015b). Therefore, the pronounced increase in D_V after carbonation may be attributed to the development of a more complex structure associated with the decomposition of C-S-H globules, the formation of $CaCO_3$, and the possible formation of a Si-rich amorphous phase in T20-C (Nirschl and Guo, 2018).

By contrast, the R_O values before and after carbonation were comparable for the T600 samples. Therefore, the higher D_V values observed for T600-C suggest that carbonation strengthened interparticle interactions and enhanced densification compared to T600. This behavior can be rationalized by the immersion of the samples in water during aqueous carbonation, which allows free water to interact with the Ca-O sites and form hydroxylated surfaces. Furthermore, amorphous silica may develop on the particle surfaces of wollastonite, which is a pyrolyzed product of C-S-H formed during thermal decomposition at 400 °C and recrystallization at 600 °C (Wang et al., 2024; Xu et al., 2023). Therefore, the increase in R_O of the thermo-activated pastes (black line in Fig. 10(b)) in the absence of CO_2 is primarily attributed to the re-adsorption of free water into the defects within the CaO layers and silicate sites, leading to the expansion of the C-S-H globules. Upon CO_2 injection, the conversion of thermo-activated C-S-H to crystalline $CaCO_3$, accompanied by the water readsorption and the formation of additional amorphous silica, results in a further increase in R_O (red line in Fig. 10(b)) (Wang et al., 2024). However, as depicted in Fig. 10(c), the extremely disrupted 3D network—evidenced by a sharp reduction in ξ_V from 2500 to 500 Å, did not recover, even after free water re-adsorption and concurrent carbonation. Fig. 10(d) shows the relative volume fractions (Φ in Eq. (4)) of the C-S-H pastes after thermo-activation, normalized to those of T20 and T20-C to elucidate the effect of thermo-activation temperature on carbonation-induced densification. The volume fraction of T20 was substantially reduced from 0.64 to 0.03 after carbonation (T20-C), which is attributed to dissolution processes during aqueous carbonation. Additionally, the volume fractions of T105 and T400 decreased relative to those of T20, indicating the formation of porous phases during the dehydration and decomposition stages (Zheng et al., 2021). By contrast, the slightly larger Φ observed for T600 compared with T20 suggests the agglomeration of C-S-H (Im et al., 2021; Zheng et al., 2021). A pronounced enhancement in the relative volume fraction was observed with increasing thermo-activation temperature, with the T600-C sample exhibiting a value up to five times higher than that of T20-C. This behavior can be ascribed to the formation of $CaCO_3$ during the aqueous carbonation, which is generally accompanied by solid volume expansion (Ma et al., 2024). In particular, the present results indicate that carbonation following thermo-activation is more

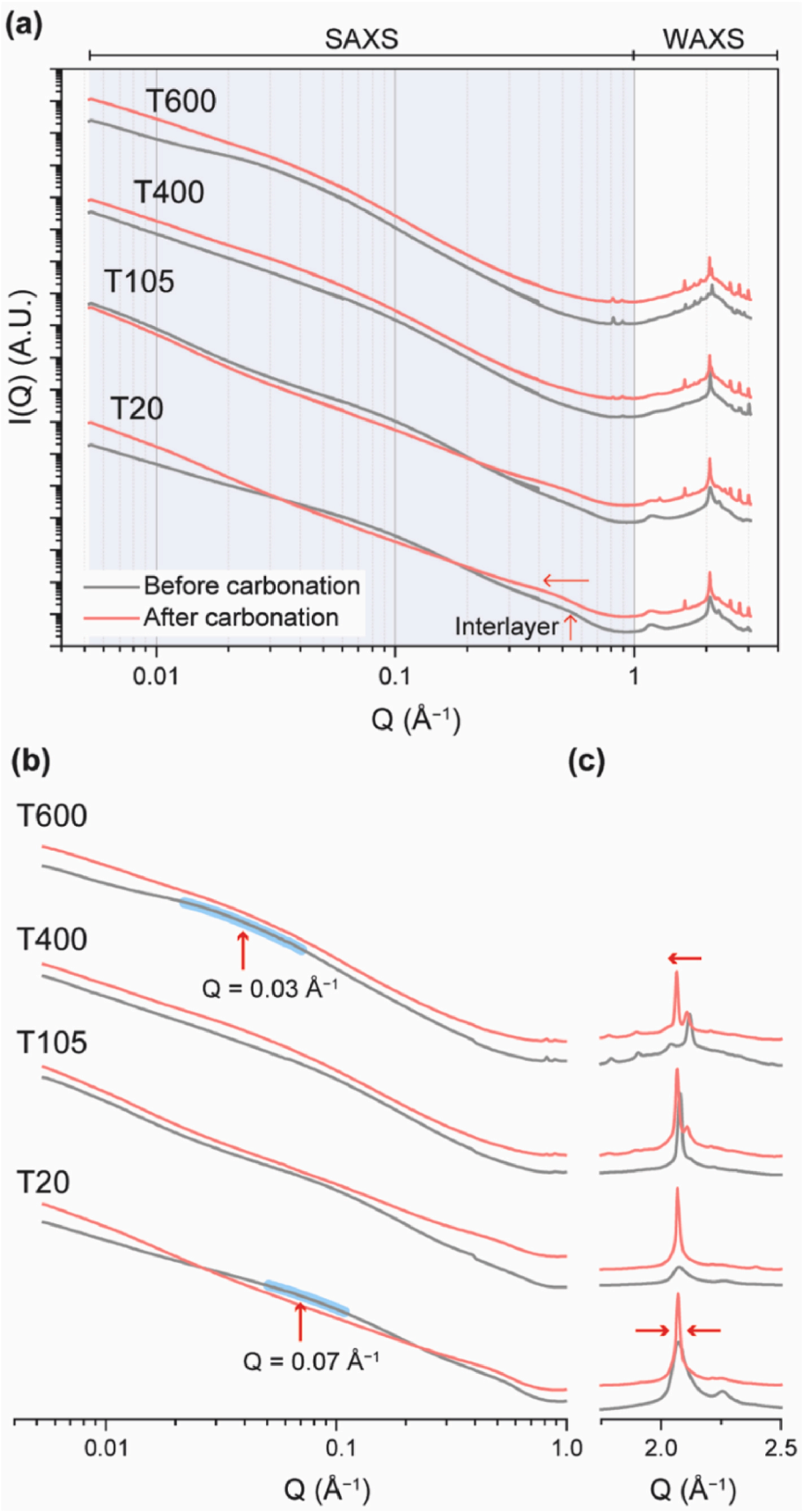

Fig. 8. Log–log plots of the X-ray scattering data for Q ranges of (a) 0.005–3 $Å^{-1}$, (b) 0.005–1 $Å^{-1}$, and (c) 1.75–2.5 $Å^{-1}$. In Fig. 8(a), the blue regions indicate the Q-ranges used for the SAXS regions.

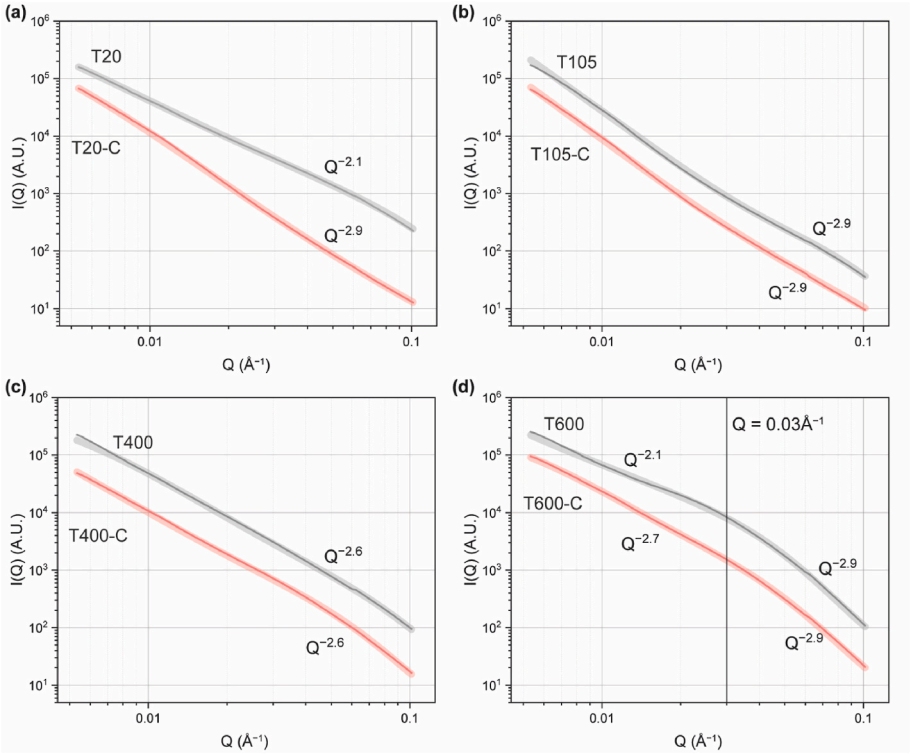

Fig. 9. Comparison of the SAXS plots and fractal fits of (a) T20 and T20-C, (b) T105 and T105-C, (c) T400 and T400-C, and (d) T600 and T600-C. The labeled $Q^{-\alpha}$ values indicate the power-law slopes of the SAXS profiles in the corresponding fractal regimes. For T600 and T600-C, the gray vertical line at $Q = 0.03\ Å^{-1}$ indicates the boundary between the two distinct power-law regimes.

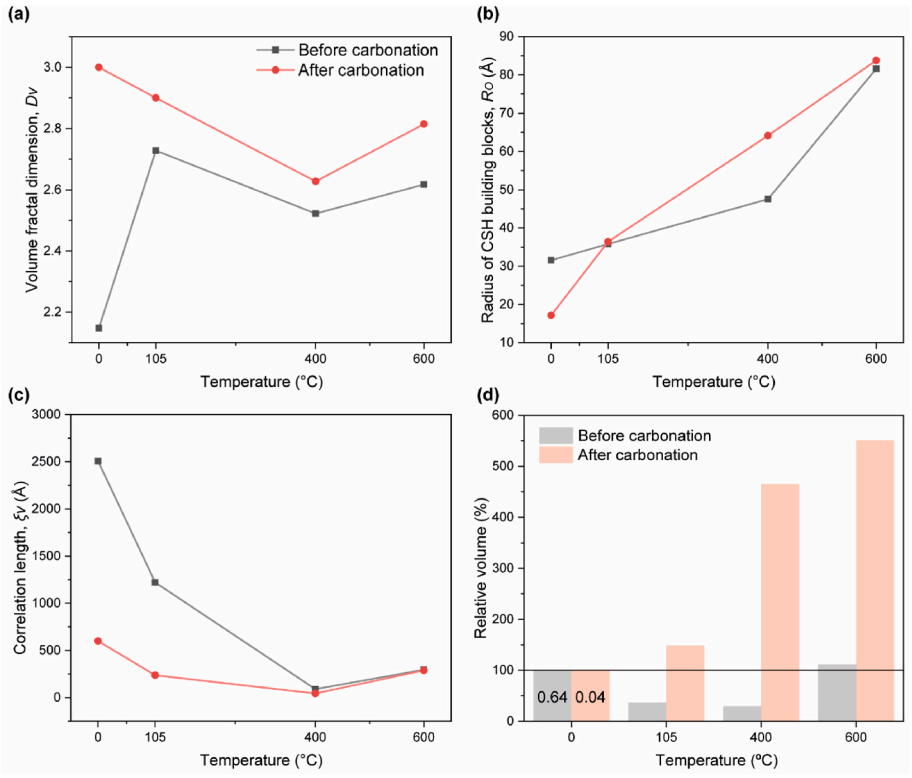

Fig. 10. Comparison of the volume-fractal fitting parameters before and after carbonation: (a) volume fractal dimension (D_V), (b) radius of C-S-H building blocks (R_O), (c) correlation length (ξ_V), and (d) relative volume fraction (Φ). D_V represents structural complexity, while R_O and ξ_V represent the building block radius and characteristic size of the fractal domains, respectively. The volume fraction of the non-carbonated and carbonated thermo-activated samples was normalized to those of T20 and T20-C, respectively.

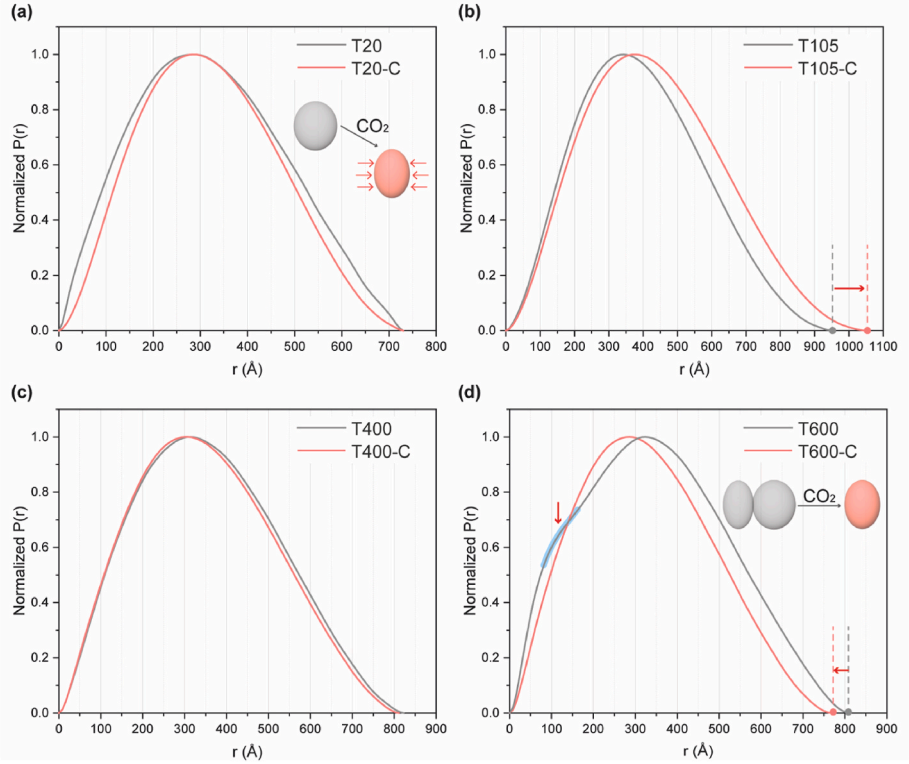

Fig. 11. Comparison of normalized *P(r)* curves of (a) T20 and T20-C, (b) T105 and T105-C, (c) T400 and T400-C, and (d) T600 and T600-C. The P(r) curves were normalized by their respective maximum values ($P_{max}(r)$). The maximum *r* value represents the maximum dimension (D_{max}) of the scattering domains within the *Q*-range of 0.005–1 $Å^{-1}$.

effective in promoting an increase in the solid volume than carbonation without prior thermal treatment because of the higher porosity of pastes and the presence of metastable C-S-H and β-wollastonite (Li et al., 2024).

Fig. 11 presents the transformed PDDFs, normalized to the maximum $P_{max}(r)$, providing information on the shape and conformational arrangement of the macromolecules (Hamley, 2021; Liu and Zwart, 2012). Asymmetrical PDDF curves were observed irrespective of thermo-activation and aqueous carbonation, suggesting that the cylindrical macromolecules (Fig. 3(c)) dominate the C-S-H globules, in agreement with results reported in previous studies (Maruyama et al., 2017; Bae et al., 2015; Li et al., 2017). Before thermo-activation, the PDDFs of T20-C exhibited slightly narrower distribution compared to that of T20 at a constant D_{max}, suggesting shrinkage of C-S-H globules induced by the dissolution of Ca^{2+} and OH^{-} (Chiang et al., 2014). In addition, the D_{max} of T105 and T400 increased to 900 and 800 Å, respectively, compared with 720 Å for T20, because the spatial distribution of C-S-H became more extended, accompanied by reduced cohesion between C-S-H globules (Bonnaud et al., 2012). After the aqueous carbonation of T105 (Fig. 11(b)), D_{max} slightly increased compared to that of T105, suggesting that CO_2 more readily penetrated the mesopores of C-S-H owing to the evaporation of free water and the presence of defects (Li et al., 2024). As the thermo-activation temperature increased to 600 °C, the development of cracks and defects within the C-S-H pastes, along with the formation of heterogeneous phases such as β-wollastonite, CaO, and amorphous silica, led to the appearance of additional peaks in the PDDFs at $r \approx 100$ Å (Fig. 11(d)) (Im et al., 2021). Upon carbonation (T600-C), the newly emerged PDDF peaks gradually merged into a single peak, indicating strengthened interaction cohesion between the solid grains in the thermo-activated C-S-H pastes. Notably, the synergistic effect of thermo-activation at 600 °C and subsequent carbonation is more effective in promoting phase densification than carbonation without prior thermo-activation, owing to the higher porosity and the presence of metastable C-S-H and β-wollastonite (Li et al., 2024). Consequently, a concomitant reduction in D_{max} was observed, indicating a more compact and unified macromolecular structure.

3.3. Changes in thermo-activated C-S-H globules after aqueous carbonation at nm–μm scale

Based on the pronounced differences observed in both the WAXS and SAXS results between (T600 and T600-C) and (T20 and T20-C), XNI was employed to further investigate the 3D structural evolution of C-S-H globules across a length scale ranging from nm to μm. As noted in the SAXS results section, vacuum drying may induce C-S-H globule shrinkage; however, all samples were subjected to the same drying protocol.

The phase assignment in the XNI images was based on grayscale contrast and morphological characteristics. The assignment of I_P and O_P C-S-H was supported by previously reported SEM-BSE observations of C-S-H synthesized using the same procedure (Kunther et al., 2017), in which grain-shaped regions and the surrounding matrix were attributed to I_P and O_P C-S-H, respectively. In addition, the characteristic morphological changes induced by thermo-activation and carbonation, as shown in Fig. S5, were considered in the interpretation of the segmented regions. As shown in the sliced X-ray nanotomography image in Fig. 12(a), the I_P and O_P C-S-H can be distinctly separated using grayscale values and morphological features. After carbonation, partial decomposition of the O_P C-S-H and the crack propagation through the I_P C-S-H occurred, resulting from carbonation shrinkage and crystal expansion (Fig. 12(b)) (Cho et al., 2024; Wan et al., 2014; Kangni-Foli et al., 2021; Seigneur et al., 2022). Furthermore, I_P C-S-H developed into a multiphase region composed of metastable C-S-H, amorphous silica, and $CaCO_3$, leading to a small variation in the grayscale values (Kangni-Foli et al., 2021). As shown in Fig. 12(c), thermally decomposed phases were predominantly observed in the O_P C-S-H rather than in the

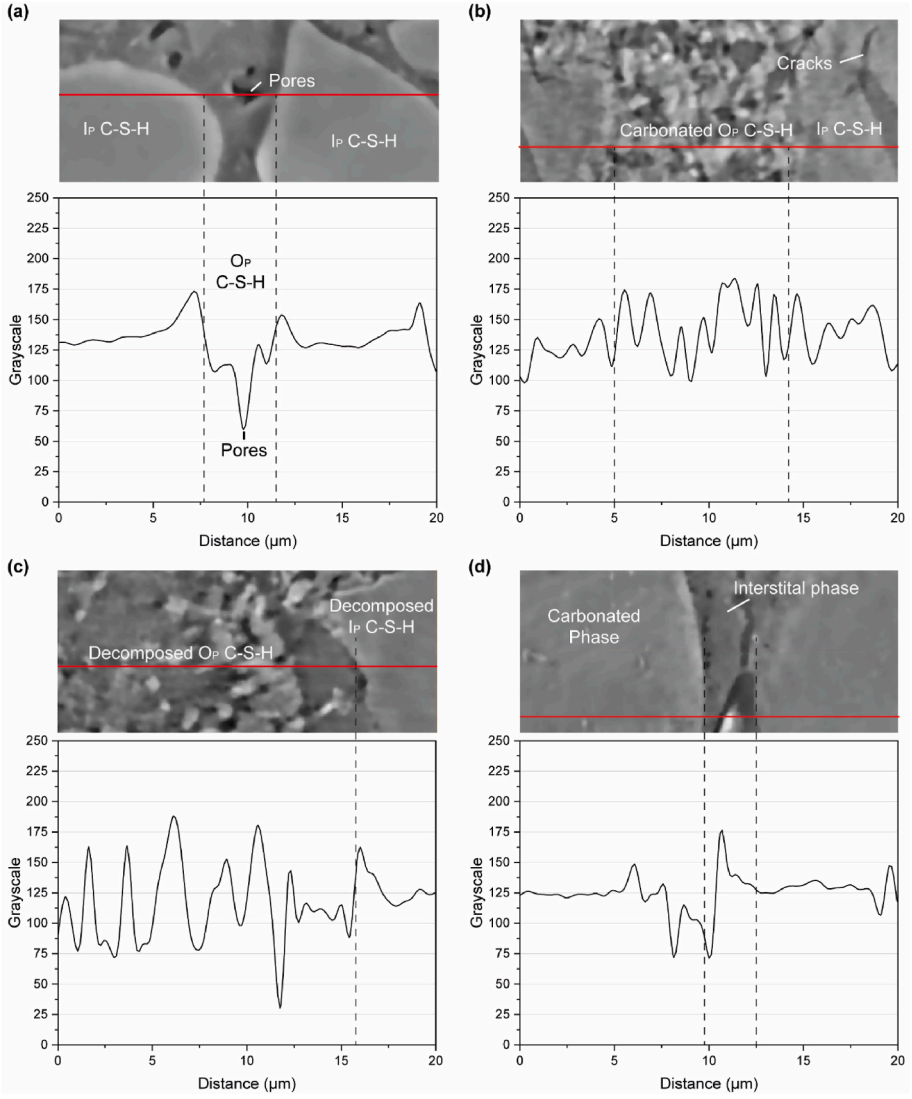

Fig. 12. Sliced X-ray nanotomography images and line probe analysis results for (a) T20, (b) T20-C, (c) T600, and (d) T600-C.

I_P C-S-H, such that the original grain morphology of the I_P C-S-H remained discernible (Zheng et al., 2021). For the T600-C samples, clearly separated phases were observed in the thermo-activated C-S-H pastes after aqueous carbonation (Fig. 12(d)). The observations in Fig. 12 are quantitatively supported by the grayscale histogram deconvolution of the VOI using Gaussian distributions (Fig. 13), which captures the evolution of the phase contrast after thermo-activation and carbonation (Suh et al., 2024c). The grayscale histogram shows multiple well-separated Gaussian peaks for T20 (Fig. 13(a)), whereas these peaks merge into a single dominant peak for T20-C (Fig. 13(b)) and T600 (Fig. 13(c)), indicating a reduced grayscale contrast between I_P C-S-H and O_P C-S-H after carbonation and thermo-activation. By contrast, for the T600-C samples, the peaks again separated (Fig. 13(d)), reflecting the re-emergence of the phase contrast associated with carbonation-induced phase evolution.

Because X-ray attenuation is influenced by the density and composition of the materials, the phase in all samples can be classified into three or more phases based on threshold values: voids, densely packed phases, and loosely packed phases (Chantler et al., 2003). The lowest threshold value corresponds to the voids in all samples. For the carbonated samples (i.e., T20-C and T600-C), the highest threshold value is associated with relatively dense $CaCO_3$-rich regions (Cho et al., 2024). Based on this phase classification, the volume fractions of voids, loosely packed phases, and densely packed phases in the VOI ($20 \times 20 \times 20\ \mu m^3$) were quantitatively evaluated, and the results are shown in Fig. 14.

As illustrated in Fig. 14(a), the IP C-S-H phase, defined by a grayscale threshold range of 121–255 in T20 (Fig. 13(a)), accounted for approximately 66% of the C-S-H paste. After thermo-activation, the void volume fraction increased to 31% in T600, which was approximately double that of T20. Simultaneously, the I_P C-S-H phase underwent substantial decomposition, resulting in a decrease in its volume fraction from 66% to 36.9%, whereas the phase associated with intermediate threshold values, representative of a relatively loosely packed structure, showed a corresponding increase. Upon the aqueous carbonation of T20 (Fig. 14(b)), the void volume fraction increased to approximately 23%, whereas almost all O_P C-S-H phases were associated with the carbonated phases corresponding to the grayscale threshold range of 147–255. In addition, the volume fraction of the second phase, corresponding to the intermediate grayscale range of 108–147, accounted for approximately 53% and was attributed to decomposed C-S-H and amorphous silica. Interestingly, as shown in Fig. 14(c), the T600-C sample was predominantly composed of a densely packed phase attributed to the carbonated phase.

Based on the phase segmentation shown in Fig. 13, the fractal dimensions of each phase were evaluated using the box-counting method,

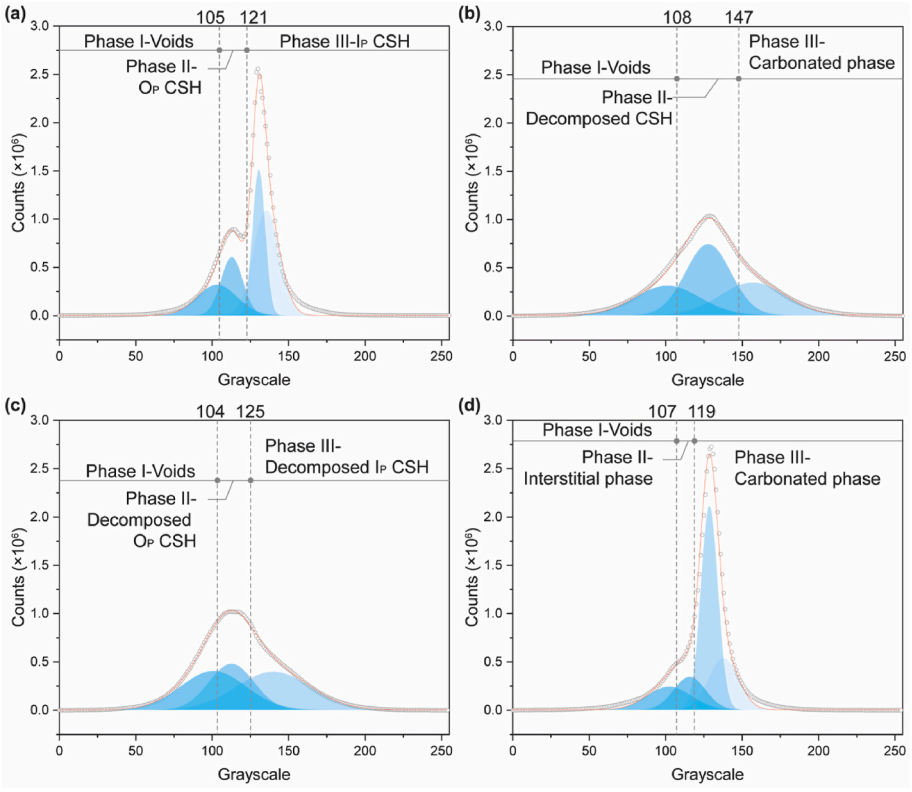

Fig. 13. Gaussian fitting results of the histogram for the VOI: (a) T20, (b) T20-C, (c) T600, and (d) T600-C.

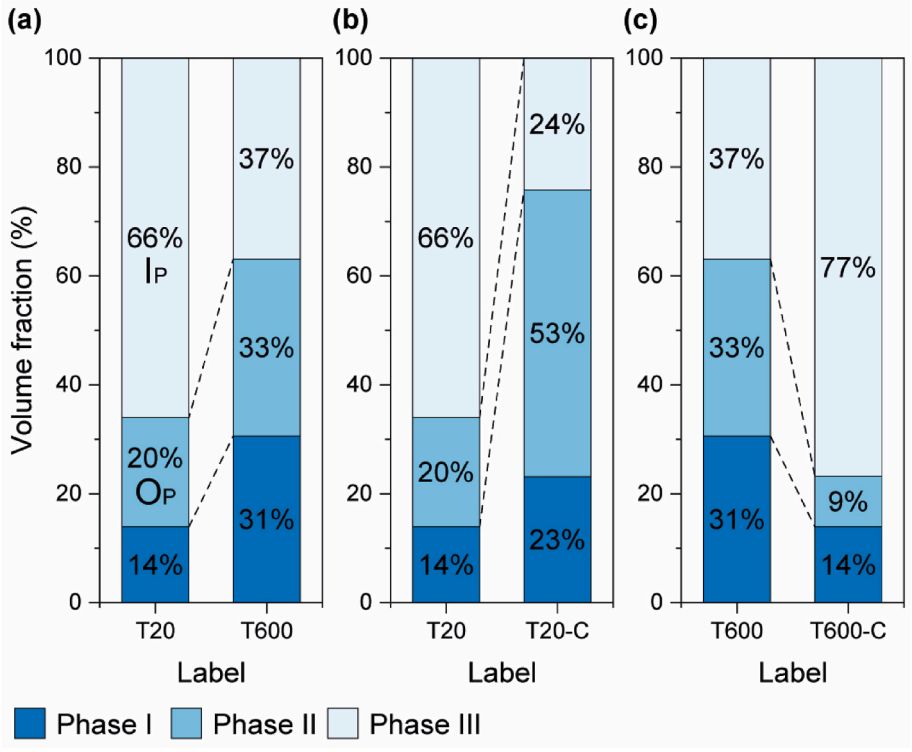

Fig. 14. Volume fraction of each phase in the VOI based on the threshold values obtained by the Gaussian fitting results, as shown in Fig. 13: (a) T20 and T600, (b) T20 and T20-C, and (c) T600 and T600-C.

and the corresponding results are shown in Fig. 15 (Yang et al., 2019). The fractal dimensions of all segmented phases increased after carbonation of T20, indicating increased surface complexity of each segmented phase. In contrast, the fractal dimensions of the segmented phases in T600 exhibited different changes after carbonation, indicating that the morphological evolution of the thermo-activated C-S-H differed from

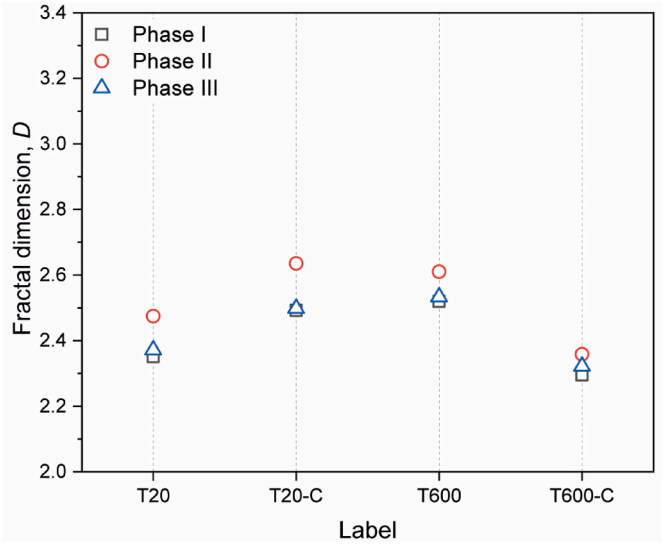

Fig. 15. 3D fractal dimension (D) of each phase obtained by XNI.

that of T20. In particular, the reduced fractal dimensions observed after carbonation can be attributed to the agglomeration of the segmented phases, which simplifies the grain surface geometry.

Fig. 16 shows the pore size distribution and cumulative pore volume as a function of the equivalent pore diameter (d_e). As reported in the previous studies, the pores can be classified according to their pore size as follows: gel pore ($d_e < 0.2$ μm), small capillary pore ($0.2\ \mu m < d_e < 2\ \mu m$), large capillary pore ($2\ \mu m < d_e < 10\ \mu m$), entrained air ($10\ \mu m < d_e < 1$ mm), and entrapped air ($d_e > 1$ mm) (Pae et al., 2024; Mehta and Monteiro, 2006). Thus, this study identified changes in the characteristics of gel pores, small capillary pores, and large capillary pores using synchrotron-based XNI according to thermo-activation and aqueous carbonation. The cumulative pore volume was the lowest in the T20 samples and increased sequentially in T600-C, T20-C, and T600 (Fig. 16(a)). This behavior can be attributed to the formation of larger capillary pores induced by thermo-activation at 600 °C, which is associated with the evaporation of moisture and chemically bound water and decomposition of I_P and O_P C-S-H. For the T20-C samples, the decomposed O_P C-S-H and crack propagation through the I_P C-S-H due to carbonation shrinkage and crystal expansion increased the cumulative pore volume in T20-C (Cho et al., 2024; Wan et al., 2014; Kangni-Foli et al., 2021; Seigneur et al., 2022). A significant reduction in cumulative pore volume was observed in T600-C samples. Notably, the maximum d_e, which was approximately 7 μm in the T600 samples, decreased to 5 μm in the T600-C, a value comparable to that of the T20 samples. As shown in Fig. 16(b), carbonation led to an increase in gel pores for T20-C compared to T20, whereas T600-C exhibited a marked decrease in gel pores relative to T600, with the change being more pronounced than that observed for small capillary pores. These results suggest that aqueous carbonation allows CO_3^{2-} species to penetrate defects within the thermo-activated C-S-H globules, leading to the densification and structural reorganization of metastable C-S-H (Li et al., 2024). Furthermore, calcite formation appears to contribute more substantially to the densification of the C-S-H layered structure, whereas capillary pores with $d_e > 0.2$ μm exhibited limited densification.

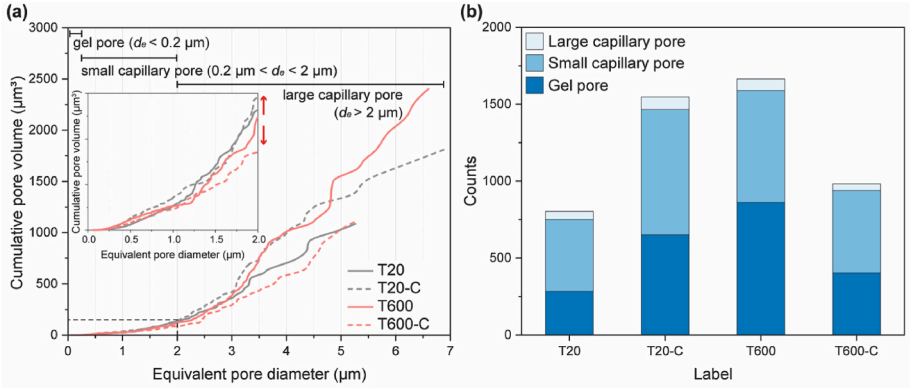

Fig. 16. (a) Cumulative pore volume comparison for T20, T20-C, T600, and T600-C; (b) quantification results of large and small capillary pores and gel pores.

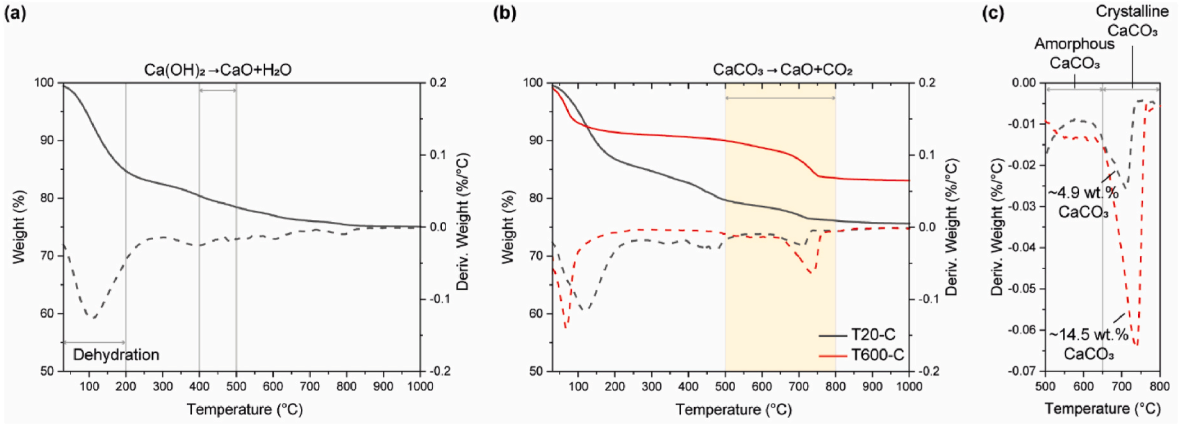

Fig. 17. TG/DTG curves of (a) T20, (b) T20-C and T600-C, and (c) enlarged DTG curves showing $CaCO_3$ decomposition in the temperature range 500–800 °C.

3.4. Quantification of CaCO3 formation by TG and Raman spectroscopy

Fig. 17 presents the TG/DTG curves of carbonated C-S-H and C-S-H thermo-activated at 600 °C, followed by aqueous carbonation (T600-C). Because evaporable water in C-S-H was removed during thermo-activation prior to aqueous carbonation, T600-C showed a substantially lower mass loss below 200 °C than T20-C. The mass loss observed in this temperature range can also be attributed to the removal of moisture adsorbed on the particle surfaces during aqueous carbonation. In T600-C, this mass loss was predominantly observed at approximately 100 °C. The DTG peak associated with $CaCO_3$ decomposition was clearly higher in T600-C than in T20-C, indicating enhanced $CaCO_3$ formation after carbonation. Notably, the sharp DTG peak observed at approximately 750 °C is attributed to the decomposition of crystalline $CaCO_3$, whereas the broad peak at a lower temperature observed only in T600-C is attributed to the decomposition of poorly crystalline $CaCO_3$ (Villain et al., 2007).

The Raman spectra of T20, T20-C, T600, and T600-C are shown in Fig. 18, and the corresponding peak assignments are summarized in Table 4 (Black et al., 2007; Garbev et al., 2007; Liu et al., 2026). The T20 sample exhibited characteristic peaks at 671, 980, and 1050 cm^{-1}, which are associated with the bending and stretching vibrations of Q^2 Si–O–Si in C-S-H (Garbev et al., 2007). After aqueous carbonation, T20-C exhibited new peaks at 278 and 1085 cm^{-1}, corresponding to the Ca–O lattice vibration and the C–O symmetric stretching vibration in $CaCO_3$ precipitates, respectively (Black et al., 2007). After thermo-activation, a pronounced fluorescence background was observed at T600, resulting in an elevated baseline. Following aqueous carbonation, the fluorescence background was substantially reduced in T600-C, accompanied by the appearance of a distinct C–O symmetric stretching band at 1085 cm^{-1} with increasing FWHM. Moreover, the Ca–O lattice vibration observed at 278 cm^{-1} in T20-C shifted to a lower Raman shift in T600-C. This shift indicates a difference in the local structural environment of $CaCO_3$, consistent with the formation of the poorly crystalline $CaCO_3$ in T600-C inferred from the TG/DTG results (Black et al., 2007).

4. Conclusions

This study investigated the initial aqueous carbonation behavior of thermo-activated C-S-H as a primary binding phase for RCPs, with the aim of elucidating the temperature-dependent structural evolution and densification mechanisms relevant to concrete waste recycling and CO_2 mineralization. Based on multiscale characterization using synchrotron-based WAXS combined with PDF, SAXS combined with fractal analysis, and XNI, the following conclusions can be drawn.

Table 4
Band assignments of Raman spectra.

Raman shift (cm^{-1})				Assignment
T20	T20-C	T600	T600-C	
	278		< 278	Lattice vibrations Ca–O (vaterite)
		315		Lattice stretching vibrations Ca–O (wollastonite)
		398		Lattice bending vibrations Ca–O (wollastonite)
		625		Si–O–Si symmetric stretching Q^2
671				Si–O–Si symmetric bending Q^2
		844		Ca–O–Si vibration
		960		Asymmetric stretching of Q^1
980				Symmetric stretching of Q^2 Si–O(H)
1050				Symmetric stretching of Q^2 Si–O(H)
	1085		1085	Symmetric stretching of C–O in $CaCO_3$ precipitates (calcite, vaterite)

- At the thermo-activation temperature below 400 °C, carbonation primarily affected C-S-H, whereas greater consumption of β-wollastonite was observed at 600 °C. Correspondingly, the extent of calcite formation progressively increased with the thermo-activation temperature, indicating increased carbonation extent after thermo-activation.
- PDF analysis revealed that carbonation induced more pronounced structural rearrangement in thermo-activated C-S-H at 600 °C than in T20, primarily affecting the long-range order of crystalline pyrolyzed phases such as β-wollastonite.
- For T20-C, the increase in D_V was accompanied by C-S-H decalcification and amorphous silica formation, along with a reduction in the R_O of the C-S-H globules. By contrast, for T600-C, the R_O values before and after carbonation, combined with a higher D_V, suggest agglomeration-associated densification of the thermo-activated C-S-H paste.
- Thermo-activation generated defects and heterogeneous phases that may promote carbonation under aqueous conditions. Following carbonation, T600-C exhibited a substantial reduction in void volume and an increase in the densely packed carbonated phase.
- The combined effects of increased porosity, the presence of metastable C-S-H, and β-wollastonite were associated with increased calcite formation and pronounced densification under aqueous carbonation conditions.

Overall, this study provides a comprehensive multiscale understanding of the early-stage carbonation behavior of thermo-activated C-S-H and provides insights into its structural evolution from Å to μm. These findings provide insights into the relative susceptibility of different thermo-activated phases to early-stage carbonation and their

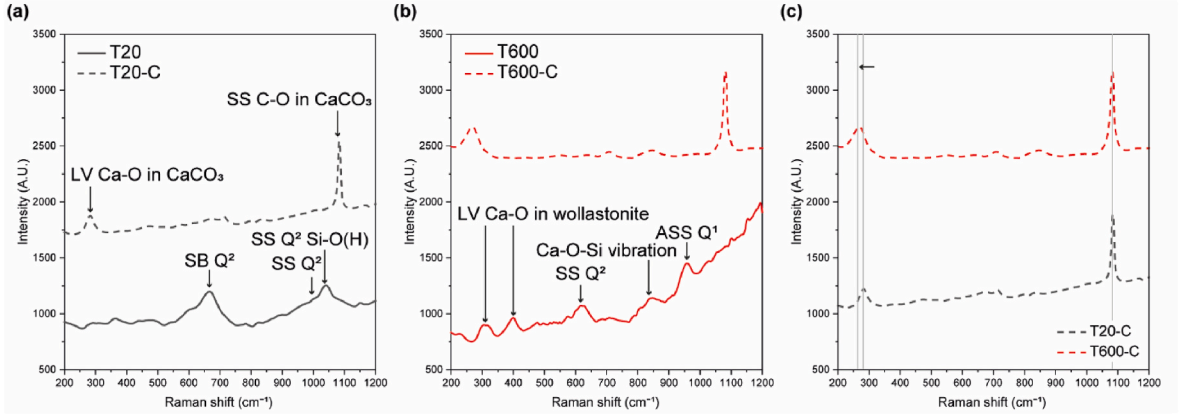

Fig. 18. Raman spectra of (a) T20 and T20-C, (b) T600 and T600-C, and (c) T20-C and T600-C, respectively.

potential roles as carbonation precursors. Nevertheless, the present study is limited to a carbonation duration of 30 min and a Ca/Si ratio of 1.0. Further studies incorporating extended carbonation durations, a wider range of Ca/Si ratios, and solution chemistry analyses, including Ca and Si concentrations and pH evolution, are required to fully elucidate the aqueous carbonation behavior of thermo-activated C-S-H.

CRediT authorship contribution statement

Sumin Im: Writing – review & editing, Writing – original draft, Visualization, Validation, Methodology, Investigation, Funding acquisition, Data curation, Conceptualization. **Seongmin Cho:** Methodology. **Gyeongryul Kim:** Investigation. **Manabu Kanematsu:** Investigation, Data curation. **Satoshi Morooka:** Software, Methodology. **Nishio Yuhei:** Software, Investigation. **Akihiko Machida:** Software, Methodology, Data curation. **Aki Tominaga:** Investigation. **Seungjun Kwon:** Methodology. **Sungchul Bae:** Writing – review & editing, Supervision, Software, Methodology, Funding acquisition, Formal analysis, Conceptualization.

Declaration of competing interest

The authors declare that they have no known competing financial interests or personal relationships that could have appeared to influence the work reported in this paper.

Acknowledgements

This study was supported by the National Research Foundation of Korea (NRF) grants funded by the Korean government (MSIT) (grant numbers NRF-2022R1A2C2010350 (RS-2022-NR070343) and RS-2025-02654027). The synchrotron-radiation X-ray diffraction experiments were performed using a QST experimental station at JAEA beamline BL22XU, SPring-8, with the approval of the Japan Synchrotron Radiation Research Institute (Proposal Nos. 2022A3784) and supported by QST Advanced Characterization Nanotechnology Platform under the remit of “Nanotechnology Platform” of the Ministry of Education, Culture, Sports, Science and Technology, Japan (Proposal Nos. JPMXP09A19QS0018, JPMXP09A20QS0021). Small-angle X-ray scattering experiments were performed at the BL4C beamline of the Pohang Accelerator Laboratory (PAL, Republic of Korea).

Appendix A. Supplementary data

Supplementary data to this article can be found online at https://doi.org/10.1016/j.dibe.2026.101049.

Data availability

Data will be made available on request.

References

Abidar, A., Bouchenafa, O., Hamzaoui, R., Mansoutre, S., Paris, M., Barnes-Davin, L., Capra, C., Classen, B., Florence, C., 2023. Investigating the mechanisms of hydraulicity regeneration in pure C3S paste. Constr. Build. Mater. 409. https://doi.org/10.1016/j.conbuildmat.2023.134132.

Ahmed, O., Ahmad, S., Adekunle, S.K., 2024. Carbon dioxide sequestration in cementitious materials: a review of techniques, material performance, and environmental impact. J. CO2 Util. 83. https://doi.org/10.1016/j.jcou.2024.102812.

Ali, Tariq, Mahmood, Muhammad Sarmad, Ahmed, Hawreen, Qureshi, Muhammad Zeeshan, Elhadi, Khaled Mohamed, Alaneme, George Uwadiegwu, Kırgız, Mehmet Serkan, Ajwad, Ali, 2026. Accelerated Carbonation Techniques of Recycled Concrete Aggregates: A Systematic Review of Methods, Effects, and Optimal Conditions. Int. J. Concrete Structures Materials 20 (1), 30. https://doi.org/10.1186/s40069-026-00907-3. https://link.springer.com/10.1186/s40069-026-00907-3. (Accessed 12 March 2026).

Allen, A.J., Thomas, J.J., Jennings, H.M., 2007. Composition and density of nanoscale calcium-silicate-hydrate in cement. Nat. Mater. 6, 311–316. https://doi.org/10.1038/nmat1871.

Anovitz, L.M., Weston, J., 2020. Exploring particle aggregation using small angle scattering techniques, crystallization via Nonclassical Pathways Volume 1: Nucleation, Assembly, Observation & Application. ACS Publications 201–257.

Aranda, M.A.G., Torre, A.G.D., Bernal, S.A., Provis, J.L., 2026. Insights into the nano- and microstructures of cementitious materials using synchrotron X-rays. Cement Concrete Res 202. https://doi.org/10.1016/j.cemconres.2026.108150.

Bae, S., Jee, H., Kanematsu, M., Shiro, A., Machida, A., Watanuki, T., Shobu, T., Suzuki, H., 2018. Pair distribution function analysis of nanostructural deformation of calcium silicate hydrate under compressive stress. J. Am. Ceram. Soc. 101, 408–418. https://doi.org/10.1111/jace.15185.

Bae, S., Jee, H., Suh, H., Kanematsu, M., Shiro, A., Machida, A., Watanuki, T., Shobu, T., Morooka, S., Geng, G.Q., Suzuki, H., 2020. Analysis of atomistic structural deformation characteristics of calcium silicate hydrate in 53-year-old tricalcium silicate paste using atomic pair distribution function. Constr. Build. Mater. 237. https://doi.org/10.1016/j.conbuildmat.2019.117714.

Bae, S., Taylor, R., Shapiro, D., Denes, P., Joseph, J., Celestre, R., Marchesini, S., Padmore, H., Tyliszczak, T., Warwick, T., Kilcoyne, D., Levitz, P., Monteiro, P.J.M., 2015. Soft X-ray ptychographic imaging and morphological quantification of calcium Silicate Hydrates (C-S-H). J. Am. Ceram. Soc. 98, 4090–4095. https://doi.org/10.1111/jace.13808.

Barzgar, S., Lothenbach, B., Tarik, M., Di Giacomo, A., Ludwig, C., 2020. The effect of sodium hydroxide on Al uptake by calcium silicate hydrates (C-S-H). J Colloid Interf Sci 572, 246–256. https://doi.org/10.1016/j.jcis.2020.03.057.

Black, L., Breen, C., Yarwood, J., Garbev, K., Stemmermann, P., Gasharova, B., 2007. Structural features of C-S-H(I) and its carbonation in air - a Raman spectroscopic study. Part II: carbonated phases. J. Am. Ceram. Soc. 90, 908–917. https://doi.org/10.1111/j.1551-2916.2006.01429.x.

Bogas, J.A., Carriço, A., Pereira, M.F.C., 2019. Mechanical characterization of thermal activated low-carbon recycled cement mortars. J. Clean. Prod. 218, 377–389. https://doi.org/10.1016/j.jclepro.2019.01.325.

Bonnaud, P.A., Ji, Q., Coasne, B., Pellenq, R.J.M., Van Vliet, K.J., 2012. Thermodynamics of water confined in porous calcium-silicate-hydrates. Langmuir 28, 11422–11432. https://doi.org/10.1021/la301738p.

Bossa, N., Chaurand, P., Vicente, J., Borschneck, D., Levard, C., Aguerre-Chariol, O., Rose, J., 2015. Micro- and nano-X-ray computed-tomography: a step forward in the characterization of the pore network of a leached cement paste. Cement Concrete Res 67, 138–147. https://doi.org/10.1016/j.cemconres.2014.08.007.

Cai, Y.X., Feng, P., Liu, X., Shen, X.Y., Lothenbach, B., 2026. Simultaneous formation and decomposition of calcium silicate hydrate under carbonation in water. Cement Concrete Res 199. https://doi.org/10.1016/j.cemconres.2025.108021.

Chantler, C.T., Olsen, K.J., Dragoset, R.A., Kishore, A.R., Kotochigova, S.A., Zucker, D.S., 2003. X-ray Form Factor, Attenuation and Scattering Tables (version 2.0).

Chiang, W.S., Ferraro, G., Fratini, E., Ridi, F., Yeh, Y.Q., Jeng, U.S., Chen, S.H., Baglioni, P., 2014. Multiscale structure of calcium- and magnesium-silicate-hydrate gels. J. Mater. Chem. A 2, 12991–12998. https://doi.org/10.1039/c4ta02479f.

Chiang, W.S., Fratini, E., Ridi, F., Lim, S.H., Yeh, Y.Q., Baglioni, P., Choi, S.M., Jeng, U.S., Chen, S.H., 2013. Microstructural changes of globules in calcium-silicate-hydrate gels with and without additives determined by small-angle neutron and X-ray scattering. J Colloid Interf Sci 398, 67–73. https://doi.org/10.1016/j.jcis.2013.01.065.

Cho, H., Lee, J., Nho, H., Lee, K., Gim, B., Lee, J., Lee, J., Ewert, K.K., Li, Y.L., Feinstein, S.C., Safinya, C.R., Jin, K.S., Choi, M.C., 2023. Synchrotron X-ray study of intrinsically disordered and polyampholytic Tau 4RS and 4RL under controlled ionic strength. European Physical Journal E 46. https://doi.org/10.1140/epje/s10189-023-00328-0.

Cho, S., Im, S., Kim, G., Suh, H., Her, S., Kanematsu, M., Machida, A., Tominaga, A., Shobu, T., Bae, S., 2026. Comparative effects of CO2-curing condition on phase assemblage and mechanical response of C3S pastes: insights from atomic, crystallographic, and macroscopic deformations. J. Build. Eng. 128. https://doi.org/10.1016/j.jobe.2026.116694.

Cho, S., Suh, H., Kim, G., Liu, J., Li, P., Bae, S., 2024. Microstructural phase evolution and strength development of low-lime calcium silicate cement (CSC) paste incorporating ordinary Portland cement under an accelerated carbonation curing environment. Constr. Build. Mater. 411. https://doi.org/10.1016/j.conbuildmat.2023.134248.

Constantinides, G., Ulm, F.-J., 2007. The nanogranular nature of C–S–H. J. Mech. Phys. Solid. 55, 64–90. https://doi.org/10.1016/j.jmps.2006.06.003.

Feng, Y., Zhong, H.C., Fang, J.D., Liu, W.S., Jiang, Z., Yang, J., Xie, J.H., 2026. NaHCO3 solution carbonation recycled powder for novel alkali-activated concrete: synergistic enhancement in mechanical properties, durability, and environmental impact. Cement Concr. Compos. 167. https://doi.org/10.1016/j.cemconcomp.2026.106465.

Garbev, K., Stemmermann, P., Black, L., Breen, C., Yarwood, J., Gasharova, B., 2007. Structural features of C-S-H(I) and its carbonation in air - a Raman spectroscopic study. Part I: fresh phases. J. Am. Ceram. Soc. 90, 900–907. https://doi.org/10.1111/j.1551-2916.2006.01428.x.

Hamley, I.W., 2021. Small-Angle Scattering: Theory, Instrumentation, Data, and Applications. John Wiley & Sons.

Han, Seongho, Kim, Jayon, Farrugia, Kay, Jun, Heejung, Borg, Ruben Paul, Kim, Jae Hong, Yoon, Jinyoung, 2026. Machine Learning-Based Prediction of Compressive Strength and CO2 Uptake in CO2-Cured Cementitious Materials. Int. J. Concrete Structures Materials 20 (1), 86. https://doi.org/10.1186/s40069-026-00956-8. https://link.springer.com/10.1186/s40069-026-00956-8. (Accessed 8 September 2026).

Her, S., Im, S., Liu, J., Suh, H., Kim, G., Sim, S., Wi, K., Park, D., Bae, S., 2024. Exploring the potential of pulverized oyster shell as a limestone substitute in limestone calcined clay cement (LC3) and its implications for performance. Constr. Build. Mater. 425. https://doi.org/10.1016/j.conbuildmat.2024.135918.

Her, S., Park, T., Zalnezhad, E., Bae, S., 2021. Synthesis and characterization of cement clinker using recycled pulverized oyster and scallop shell as limestone substitutes. J. Clean. Prod. 278. https://doi.org/10.1016/j.jclepro.2020.123987.

Huang, J.Y., Chen, Y.X., Yu, Q.L., 2025. Amorphous calcium carbonate formation from carbonated recycled cement powder: a novel carbonation-activated cementitious material. Compos Part B-Eng 297. https://doi.org/10.1016/j.compositesb.2025.112336.

Ilavsky, J., Jemian, P.R., 2009. Irena: tool suite for modeling and analysis of small-angle scattering. J. Appl. Crystallogr. 42, 347–353. https://doi.org/10.1107/S0021889809002222.

Im, S., Jee, H., Kanematsu, M., Morooka, S., Choe, H., Yuhei, N., Machida, A., Tominaga, A., Jeon, B., Bae, S., 2025. Multi-scale synchrotron X-ray scattering studies on thermo-induced changes in structural and mechanical properties of CSH/PCE composites. Constr. Build. Mater. 459. https://doi.org/10.1016/j.conbuildmat.2024.139742.

Im, S., Jee, H., Suh, H., Kanematsu, M., Morooka, S., Choe, H., Yuhei, N., Machida, A., Kim, J., Lim, S., Bae, S., 2023. Insight on the mechanical properties of hierarchical porous calcium-silicate-hydrate pastes according to the Ca/Si molar ratio using synchrotron X-ray scattering and nanoindentation test. Constr. Build. Mater. 365. https://doi.org/10.1016/j.conbuildmat.2022.130034.

Im, S., Jee, H., Suh, H., Kanematsu, M., Morooka, S., Taku, K., Yuhei, N., Machida, A., Kim, J., Bae, S., 2021. Temperature effects on local structure, phase transformation, and mechanical properties of calcium silicate hydrates. J. Am. Ceram. Soc. 104, 4803–4818. https://doi.org/10.1111/jace.17881.

Jiang, Y., Peng, L.G., Ma, Z.H., Lu, J.X., Shen, P.L., Poon, C.S., 2023. Enhancing the treatment efficiency of recycled concrete fines with aqueous carbonation. Cement Concrete Res 174. https://doi.org/10.1016/j.cemconres.2023.107338.

Kangni-Foli, E., Poyet, S., Le Bescop, P., Charpentier, T., Bernachy-Barbé, F., Dauzères, A., L'Hôpital, E., De Lacaillerie, J.B.D., 2021. Carbonation of model cement pastes: the mineralogical origin of microstructural changes and shrinkage. Cement Concrete Res 144. https://doi.org/10.1016/j.cemconres.2021.106446.

Kim, C., Jarumaneeroj, C., Rungswang, W., Jin, K.S., Ree, M., 2022b. A comprehensive small angle X-ray scattering analysis on morphological structure of semicrystalline linear polymer in bulk state. Polymer 243. https://doi.org/10.1016/j.polymer.2022.124610.

Kim, G., Im, S., Jee, H., Suh, H., Cho, S., Kanematsu, M., Morooka, S., Koyama, T., Nishio, Y., Machida, A., Kim, J., Bae, S., 2022a. Effect of magnesium silicate hydrate (M-S-H) formation on the local atomic arrangements and mechanical properties of calcium silicate hydrate (C-S-H): in situ X-ray scattering study. Cement Concrete Res 159. https://doi.org/10.1016/j.cemconres.2022.106869.

Kim, J.H., Min, B., Yun, Y.D., Choi, H.J., Jin, K.S., 2020. Size-Exclusion chromatography coupled with small-angle x-ray scattering on the 4C small-angle x-ray scattering beamline at Pohang Light source II. Bull. Kor. Chem. Soc. 41.

Kim, K., Kim, J., Yun Young, D., Hyungu, A., Min Byoung, S., Kim, N., Seungyu, R., Hyo-yun, K., Lee, C., Seo, I., Woulwoo, L., Hyeong Joo, C., Kyeong Sik, J., 2017. Small-angle X-ray scattering beamline BL4C SAXS at Pohang Light source II. Biodesign 5, 24–29.

Kunther, W., Ferreiro, S., Skibsted, J., 2017. Influence of the Ca/Si ratio on the compressive strength of cementitious calcium-silicate-hydrate binders. J. Mater. Chem. A 5, 17401–17412. https://doi.org/10.1039/c7ta06104h.

Kupwade-Patil, K., Chin, S., Ilavsky, J., Andrews, R.N., Bumajdad, A., Büyüköztürk, O., 2018. Hydration kinetics and morphology of cement pastes with pozzolanic volcanic ash studied via synchrotron-based techniques. J. Mater. Sci. 53, 1743–1757. https://doi.org/10.1007/s10853-017-1659-4.

Li, B.Y., Ma, Y.F., He, J.H., Mu, S., Zhao, H.T., Zhuang, Z.J., Li, W.W., Yang, H.M., Zhang, Z., Gu, Q., Wu, H., Jin, M., Liu, J.P., 2025. Wet carbonation of calcium silicate hydrate (C-S-H): structural transformation and calcium carbonate crystallization pathways. J. Build. Eng. 113. https://doi.org/10.1016/j.jobe.2025.114090.

Li, G., Tao, Y., Zhu, X.P., Gao, Y.N., Shen, P.L., Yin, B.B., Dupuis, R., Ioannidou, K., Pellenq, R.J.M., Poon, C.S., 2024. Optimal CO2 intake in metastable water film in mesoporous materials. Nat. Commun. 15. https://doi.org/10.1038/s41467-024-55125-w.

Li, H., Du, T., Xiao, H.G., Zhang, Q.Q., 2017. Crystallization of calcium silicate hydrates on the surface of nanomaterials. J. Am. Ceram. Soc. 100, 3227–3238. https://doi.org/10.1111/jace.14842.

Li, J., Yu, Q., Huang, H., Yin, S., 2019. Effects of Ca/Si ratio, aluminum and magnesium on the carbonation behavior of calcium silicate hydrate. Materials 12, 1268.

Li, T., Senesi, A.J., Lee, B., 2016. Small angle X-ray scattering for nanoparticle research. Chem. Rev. 116, 11128–11180. https://doi.org/10.1021/acs.chemrev.5b00690.

Li, X.R., Ouzia, A., Scrivener, K., 2018. Laboratory synthesis of C3S on the kilogram scale. Cement Concrete Res 108, 201–207. https://doi.org/10.1016/j.cemconres.2018.03.019.

Li, X.R., Scrivener, K.L., 2025. Quantification of nano-crystalline C-S-H in hydrated tricalcium silicate, Portland cement and fly ash cement using PONKCS method. Cement Concrete Res 191. https://doi.org/10.1016/j.cemconres.2025.107837.

Liu, H.G., Zwart, P.H., 2012. Determining pair distance distribution function from SAXS data using parametric functionals. J. Struct. Biol. 180, 226–234. https://doi.org/10.1016/j.jsb.2012.05.011.

Liu, S.H., Zhang, L., Xuan, D.X., Shen, P.L., Zhu, J.P., Guan, X.M., Shi, C.J., 2021. Enhanced carbonation reactivity of wollastonite by rapid cooling process: towards an ultra-low calcium CO2 sequestration binder. Constr. Build. Mater. 299. https://doi.org/10.1016/j.conbuildmat.2021.124336.

Liu, X., Feng, P., Cai, Y.X., Yu, X.H., Liu, Q., 2022b. Carbonation behaviors of calcium silicate hydrate (C-S-H): effects of aluminum. Constr. Build. Mater. 325. https://doi.org/10.1016/j.conbuildmat.2022.126825.

Liu, X., Feng, P., Cai, Y.X., Yu, X.H., Yu, C., Ran, Q.P., 2022a. Carbonation behavior of calcium silicate hydrate (C-S-H): its potential for CO2 capture. Chem. Eng. J. 431. https://doi.org/10.1016/j.cej.2021.134243.

Liu, Y.H., Li, B., Chen, W., Lu, Z.C., Ouyang, L.Z., 2026. Green cement from wollastonite (CaO·SiO2) through mechanochemical method. Constr. Build. Mater. 533. https://doi.org/10.1016/j.conbuildmat.2026.146827.

Ma, Y.F., Jin, M., Wang, F., Jacques, D., Shen, X.Y., Zhang, J., Gao, C., Zeng, H.Y., Liu, J. W., Liu, J.P., 2025. Heating-induced transformations in calcium silicate hydrate (C-S-H): In-situ investigations of composition, structure, and morphology. Cement Concrete Res 190. https://doi.org/10.1016/j.cemconres.2025.107819.

Ma, Z.H., Jiang, L., Jiang, Y., Shen, P.L., Tao, Y., Li, J.S., Poon, C.S., 2024. Utilizing waste cement for carbon dioxide sequestration and capture: the role of water content on the growth of calcium carbonate. Acs Sustain Chem Eng 12, 2273–2288. https://doi.org/10.1021/acssuschemeng.3c06700.

Mao, Y.G., He, P.P., Drissi, S., Zhang, J., Hu, X., Shi, C.J., 2023. Effect of conditions on wet carbonation products of recycled cement paste powder. Cement Concr. Compos. 144. https://doi.org/10.1016/j.cemconcomp.2023.105307.

Mao, Y.G., Hu, X., Alengaram, U.J., Chen, W., Shi, C.J., 2024. Use of carbonated recycled cement paste powder as a new supplementary cementitious material: a critical review. Cement Concr. Compos. 154. https://doi.org/10.1016/j.cemconcomp.2024.105783.

Mardani, A., Bui, N.K., Noguchi, T., 2024. Hybrid environmentally friendly method for RCA concrete quality improvement. Int. J. Concr. Struct. Mater. 18. https://doi.org/10.1186/s40069-024-00664-1.

Maruyama, I., Sakamoto, N., Matsui, K., Igarashi, G., 2017. Microstructural changes in white Portland cement paste under the first drying process evaluated by WAXS, SAXS, and USAXS. Cement Concrete Res 91, 24–32. https://doi.org/10.1016/j.cemconres.2016.10.002.

Mehta, P.K., Monteiro, P., 2006. Concrete: Microstructure, Properties, and Materials (No Title).

Moore, P.B., 1980. Small-Angle scattering - information-content and error analysis. J. Appl. Crystallogr. 13, 168–175. https://doi.org/10.1107/S002188988001179x.

Morandeau, A.E., White, C.E., 2015. In situ X-ray pair distribution function analysis of accelerated carbonation of a synthetic calcium-silicate-hydrate gel. J. Mater. Chem. A 3, 8597–8605. https://doi.org/10.1039/c5ta00348b.

Naber, C., Stegmeyer, S., Jansen, D., Goetz-Neunhoeffer, F., Neubauer, J., 2019. The PONKCS method applied for time resolved XRD quantification of supplementary cementitious material reactivity in hydrating mixtures with ordinary Portland cement. Constr. Build. Mater. 214, 449–457. https://doi.org/10.1016/j.conbuildmat.2019.04.157.

Nirschl, H., Guo, X.A., 2018. Characterisation of structured and functionalised particles by small-angle X-ray scattering (SAXS). Chem. Eng. Res. Des. 136, 431–446. https://doi.org/10.1016/j.cherd.2018.06.012.

Pae, J., Kang, H.Y.N., Moon, J., 2024. Computational model to estimate chloride diffusivity by ternary random walk simulation on tomographic 3D microstructure of cement matrix. Constr. Build. Mater. 411. https://doi.org/10.1016/j.conbuildmat.2023.134349.

Pan, S.Y., Chen, Y.H., Fan, L.S., Kim, H., Gao, X., Ling, T.C., Chiang, P.C., Pei, S.L., Gu, G. W., 2020. CO2 mineralization and utilization by alkaline solid wastes for potential carbon reduction. Nat. Sustain. 3, 399–405. https://doi.org/10.1038/s41893-020-0486-9.

Poon, C.S., Shen, P.L., Jiang, Y., Ma, Z.H., Xuan, D.X., 2023. Total recycling of concrete waste using accelerated carbonation: a review. Cement Concrete Res 173. https://doi.org/10.1016/j.cemconres.2023.107284.

Sagar, C., Sharma, U.K., 2025. Role of concrete design parameters in preventing corrosion-driven failures in reinforced concrete structures. J. Struct. Integrity Maint. 10. https://doi.org/10.1080/24705314.2025.2557075.

Seifu, Melaku N., Adem, Jemal Kedir, Khalid, Hammad R., Kim, G.M., Park, Solmoi, 2025. Effects of Water-to-Binder Ratios on the Workability, Durability and Strength Development of In-Situ Carbonated Concrete. Int. J. Concrete Structures Materials 19 (1), 96. https://doi.org/10.1186/s40069-025-00827-8. https://link.springer.com/10.1186/s40069-025-00827-8. (Accessed 16 October 2025).

Seifu, M.N., Adem, J.K., Khalid, H.R., Kim, G.M., Park, S., 2025. Effects of water-to-binder ratios on the workability, durability and strength development of In-Situ carbonated concrete. Int. J. Concr. Struct. Mater. 19. https://doi.org/10.1186/s40069-025-00827-8.

Seigneur, N., De Windt, L., Poyet, S., Socié, A., Dauzères, A., 2022. Modelling of the evolving contributions of gas transport, cracks and chemical kinetics during atmospheric carbonation of hydrated C3S and C-S-H pastes. Cement Concrete Res 160. https://doi.org/10.1016/j.cemconres.2022.106906.

Semugaza, G., Mielke, T., Castillo, M.E., Gierth, A.Z., Tam, J.X., Nawrath, S., Lupascu, D. C., 2023. Reactivation of hydrated cement powder by thermal treatment for partial replacement of ordinary portland cement. Mater. Struct. 56. https://doi.org/10.1617/s11527-023-02133-9.

Sevelsted, T.F., Skibsted, J., 2015a. Carbonation of C-S-H and C-A-S-H samples studied by C, Al and Si MAS NMR spectroscopy. Cement Concrete Res 71, 56–65. https://doi.org/10.1016/j.cemconres.2015.01.019.

Sevelsted, T.F., Skibsted, J., 2015b. Carbonation of C-S-H and C-A-S-H samples studied by 13C, 27Al and 29Si MAS NMR spectroscopy. Cement Concrete Res 71, 56–65. https://doi.org/10.1016/j.cemconres.2015.01.019.

Shui, Z.H., Xuan, D.X., Chen, W., Yu, R., Zhang, R., 2009. Cementitious characteristics of hydrated cement paste subjected to various dehydration temperatures. Constr. Build. Mater. 23, 531–537. https://doi.org/10.1016/j.conbuildmat.2007.10.016.

Shui, Z.H., Xuan, D.X., Wan, H.W., Cao, B.B., 2008. Rehydration reactivity of recycled mortar from concrete waste experienced to thermal treatment. Constr. Build. Mater. 22, 1723–1729. https://doi.org/10.1016/j.conbuildmat.2007.05.012.

Suh, H., Cho, S., Im, S., Moon, J., Park, J., Lim, J., Nezhad, E.Z., Seok, S., Bae, B.I., Bae, S., 2024a. Characterization of thermal resistance and mechanical strength recovery of carbon nanotubes incorporated Portland cement composites subjected to heating and rehydration: visualization of pore structural evolutions via synchrotron 3D X-ray nanoimaging. Cement Concr. Compos. 146. https://doi.org/10.1016/j.cemconcomp.2023.105361.

Suh, H., Cho, S., Kim, G., Bae, S., 2024b. Quantitative characterization of nano-scale pore structures in a consistent volume of cement paste subjected to heating via synchrotron X-ray nanoimaging. Cement Concrete Res 185. https://doi.org/10.1016/j.cemconres.2024.107630.

Suh, H., Im, S., Kim, J., Bae, S., 2022. Instant mechanical recovery of heat-damaged nanosilica-incorporated cement composites under various rehydrations procedures. Mater. Struct. 55. https://doi.org/10.1617/s11527-021-01847-y.

Suh, H., Jee, H., Kim, J., Kitagaki, R., Ohki, S., Woo, S., Jeong, K., Bae, S., 2020. Influences of rehydration conditions on the mechanical and atomic structural recovery characteristics of Portland cement paste exposed to elevated temperatures. Constr. Build. Mater. 235. https://doi.org/10.1016/j.conbuildmat.2019.117453.

Suh, H., Kim, G., Im, S., Park, J., Bae, S., 2024c. A mechanism study of thermal resistance formation and post-fire strength recovery in cement paste with carbon nanotubes and nanosilica via focused ion beam/scanning electron microscopy tomography. J. Build. Eng. 97. https://doi.org/10.1016/j.jobe.2024.110750.

Thomas, J.J., Allen, A.J., Jennings, H.M., 2008. Structural changes to the calcium-silicate-hydrate gel phase of hydrated cement with Age, drying, and resaturation. J. Am. Ceram. Soc. 91, 3362–3369. https://doi.org/10.1111/j.1551-2916.2008.02636.x.

Trapote-Barreira, A., Porcar, L., Cama, J., Soler, J.M., Allen, A.J., 2015. Structural changes in C-S-H gel during dissolution: Small-angle neutron scattering and Si-NMR characterization. Cement Concrete Res 72, 76–89. https://doi.org/10.1016/j.cemconres.2015.02.009.

Truong, G.T., Roh, Y.S., Huynh, T.C., Nguyen, T.P., 2025. Estimating punching shear strength of recycled aggregate reinforced concrete flat slabs. J. Struct. Integrity Maint. 10. https://doi.org/10.1080/24705314.2025.2465180.

Villain, G., Thiery, M., Platret, G., 2007. Measurement methods of carbonation profiles in concrete: thermogravimetry, chemical analysis and gammadensimetry. Cement Concrete Res 37, 1182–1192. https://doi.org/10.1016/j.cemconres.2007.04.015.

Wan, K.S., Xu, Q., Wang, Y.D., Pan, G.H., 2014. 3D spatial distribution of the calcium carbonate caused by carbonation of cement paste. Cement Concr. Compos. 45, 255–263. https://doi.org/10.1016/j.cemconcomp.2013.10.011.

Wang, G., Qin, X.J., Shen, J.N., Zhang, Z.Y., Han, D.Y., Jiang, C.H., 2019. Quantitative analysis of microscopic structure and gas seepage characteristics of low-rank coal based on CT three-dimensional reconstruction of CT images and fractal theory. Fuel 256. https://doi.org/10.1016/j.fuel.2019.115900.

Wang, J.J., Mu, M.L., Liu, Y.L., 2018. Recycled cement. Constr. Build. Mater. 190, 1124–1132. https://doi.org/10.1016/j.conbuildmat.2018.09.181.

Wang, J.W., Yang, R.X., Sanz-Camacho, P., Duttine, M., Huthwelker, T., Li, J.Q., 2026. Aluminum incorporation lowers the intrinsic mechanical properties of single-chain calcium silicate hydrate. Cement Concrete Res 199. https://doi.org/10.1016/j.cemconres.2025.108026.

Wang, T., Tang, W.J., Zhang, W., Yi, Z.W., Guo, R.N., Zhang, L., Luo, K., Fan, W.Y., Gao, X., 2024. Effect of surface water on wollastonite carbonation: activated dissolution and mass transfer. Chem. Eng. J. 485. https://doi.org/10.1016/j.cej.2024.149324.

Wang, Y.S., Zhang, H.Z., Park, K.B., Eun, H., Lin, R.S., Wang, X.Y., 2025. Utilizing CO2-activated wollastonite to develop sustainable ternary composite material: CO2 utilization, performance evaluation, and mechanism analysis. Constr. Build. Mater. 492. https://doi.org/10.1016/j.conbuildmat.2025.142973.

Wu, H.X., Gao, J.M., Liu, C., Luo, X., Chen, G.F., 2024. Combine use of 100% thermoactivated recycled cement and recycled aggregate for fully recycled mortar: properties evaluation and modification. J. Clean. Prod. 450. https://doi.org/10.1016/j.jclepro.2024.141841.

Xi, X.Y., Zheng, Y.X., Zhuo, J.B., Zhang, P., Golewski, G.L., Du, C.W., 2024. Mechanical properties and hydration mechanism of nano-silica modified alkali-activated thermally activated recycled cement. J. Build. Eng. 98. https://doi.org/10.1016/j.jobe.2024.110998.

Xie, F., Gao, W., Li, C., Ren, Q., Jiang, Z., Snellings, R., 2026. Mechanistic insights into the aqueous carbonation of calcium silicate glasses: coupling of disordered network structure, dissolution kinetics and carbonation reactivity. Cement Concrete Res 209, 108364.

Xu, L., Wang, J.J., Li, K.F., Hao, T.Y., Li, Z., Li, L., Ran, B., Du, H., 2023. New insights on dehydration at elevated temperature and rehydration of GGBS blended cement. Cement Concr. Compos. 139. https://doi.org/10.1016/j.cemconcomp.2023.105068.

Yang, X., Zhang, R.J., Ma, S., Yang, X.C., Wang, F.L., 2019. Fractal dimension of concrete meso-structure based on X-ray computed tomography. Powder Technol. 350, 91–99. https://doi.org/10.1016/j.powtec.2019.03.003.

Yu, Q., Tang, J.H., Wang, G.L., Zhao, D.W., Yang, C.F., 2026. Enhancement of mechanical properties and strengthening mechanism of fully recycled aggregate concrete via calcium-based composite mineralization. Int. J. Concr. Struct. Mater. 20. https://doi.org/10.1186/s40069-025-00882-1.

Zajac, M., Maruyama, I., Iizuka, A., Skibsted, J., 2023. Enforced carbonation of cementitious materials. Cement Concrete Res 174. https://doi.org/10.1016/j.cemconres.2023.107285.

Zajac, M., Skibsted, J., Ben Haha, M., 2021a. Effect of alkalis on enforced carbonation of cement paste: mechanism of reaction. J. Am. Ceram. Soc. 104, 1076–1087. https://doi.org/10.1111/jace.17481.

Zajac, M., Skibsted, J., Durdzinski, P., Ben Haha, M., 2021b. Effect of alkalis on products of enforced carbonation of cement paste. Constr. Build. Mater. 291. https://doi.org/10.1016/j.conbuildmat.2021.123203.

Zajac, M., Skibsted, J., Durdzinski, P., Bullerjahn, F., Skocek, J., Ben Haha, M., 2020b. Kinetics of enforced carbonation of cement paste. Cement Concrete Res 131. https://doi.org/10.1016/j.cemconres.2020.106013.

Zajac, M., Skibsted, J., Skocek, J., Durdzinski, P., Bullerjahn, F., Ben Haha, M., 2020a. Phase assemblage and microstructure of cement paste subjected to enforced, wet carbonation. Cement Concrete Res 130. https://doi.org/10.1016/j.cemconres.2020.105990.

Zhai, W.Q., Sun, R.M., Xie, Y.D., Ding, H.C., Su, Y.L., He, Z.H., 2025. Thermal-activated recycled cement powder synergized with fly ash as supplementary cementitious in Portland cement: strength, microstructure and environmental benefits. Constr. Build. Mater. 474. https://doi.org/10.1016/j.conbuildmat.2025.141018.

Zheng, Q., Jiang, J.Y., Li, X.L., Bustillo, K.C., Zheng, H.M., 2021. In situ TEM observation of calcium silicate hydrate nanostructure at high temperatures. Cement Concrete Res 149. https://doi.org/10.1016/j.cemconres.2021.106579.

Zheng, Y.X., Xi, X.Y., Liu, H., Du, C.W., Lu, H.B., 2024. A review: enhanced performance of recycled cement and CO2 emission reduction effects through thermal activation and nanosilica incorporation. Constr. Build. Mater. 422. https://doi.org/10.1016/j.conbuildmat.2024.135763.